AN ANISOTROPIC ADAPTIVE PROCEDURE FOR EFFICIENT BLOOD FLOW SIMULATIONS

By

Onkar Sahni

A Thesis Submitted to the Graduate

Faculty of Rensselaer Polytechnic Institute

in Partial Fulfillment of the

Requirements for the Degree of

MASTER OF SCIENCE

Approved:

Dr. Kenneth E. Jansen, Thesis Adviser

Dr. Mark S. Shephard, Thesis Adviser

Rensselaer Polytechnic Institute
Troy, New York

December 2004
(For Graduation December 2004)

CONTENTS

LIST OF TABLES

LIST OF FIGURES

ACKNOWLEDGMENT

I would like to express my sincere gratitude to my advisors, Professor Kenneth E. Jansen and Professor Mark S. Shephard, for their support and guidance throughout this work. Their insightful advice, constant encouragement and consistent patience have been essential for the successful completion of this work. Invigorating work environment and excellent resources provided by them at SCOREC was also instrumental towards the completion of this work. I would also like to express my appreciation to them for their valuable inputs to improve the overall quality of this thesis.

I would like to thank my colleagues, Frédéric Alauzet and Jens Müller, for their useful suggestions in the course of this work and for their time in reading this thesis. I would also like to thank my friends and fellow graduate students, Arun, Manas, Mohan and Viswanath, for their fruitful discussions in general. I also want to mention that working with various people at SCOREC gave me a lot of pleasure.

I would like to express my sincerest appreciation to Gulshan uncle, Ashweni uncle and Usha aunt for their moral support; and also for their financial support during my first year at RPI. Last, but certainly not least, I would like to thank my parents for their ceaseless love and encouragement over the years.

ABSTRACT

Directional features like boundary layers commonly arise in the solution of partial differential equations governing fluid flows. Such features can be resolved efficiently by using anisotropic meshes. To automatically construct such a mesh requires an adaptive algorithm that provides information about the desired anisotropic mesh size field. In recent years, several researchers have considered and investigated procedures to construct anisotropic size field. To compute anisotropic element sizes over the domain we adopt the Hessian strategy. In this work, the Hessian strategy is based on the second derivatives of average flow field over a cardiac cycle due to the pulsatile nature of the flow in blood vessels.

This study presents an algorithm to perform anisotropic mesh adaptation in the simulation of blood flow in the cardiovascular system. The governing equations are the transient incompressible Navier-Stokes equations. We first apply the procedure to analytical cases and then to a real case of porcine aorta with a stenosis bypassed by a graft that involves real 3D curved geometry of blood vessels. We demonstrate that such a method results in an order of magnitude reduction in the computing time for a given level of accuracy making the method computationally efficient.

One of the quantities of physical interest in blood flow simulations is the wall shear stress (WSS). In this study we investigate the effect of the quality of meshes, obtained through anisotropic adaptive procedure, on WSS predictions. We demonstrate that controlling the mesh adaptation procedure in a way that maintains structured and graded elements near the wall leads to a more accurate WSS computation.

CHAPTER 1
INTRODUCTION

1.1 Background and Motivation

The dramatic increase in computational power has enabled numerical simulations of a wide range of physical problems, including fluid mechanics, as a cost-effective way for understanding the physical problem at hand. In recent years, significant effort has been spent in the field of hemodynamics to simulate blood flow in the cardiovascular system. The relationship between hemodynamic factors and arterial diseases has attracted numerous investigators to study arterial blood flow and wall shear stress (WSS) patterns. The direct application of such a relationship will help in surgical planning, in which patient-specific anatomic and physiologic information can be used to predict changes in blood flow for alternative surgical procedures [43].

Interesting challenges arise in blood flow simulations due to transient and non-linear nature of the problem involving 3D complex geometries. Finite element (FE) methods provide a viable option for understanding the complex nature of blood flow in realistic geometry (i.e., patient-specific geometry) and for obtaining relevant flow quantities, like WSS. FE method falls under the class of numerical methods used for constructing *approximate* solutions of well defined partial differential equations. In FE methods the physical domain is discretized into a finite collection of elements called a mesh. The solution of the problem is then approximated on each element. In order to employ the FE method to simulate blood flow the geometric model, representing blood vessels, has to be subdivided into a finite number of elements. The obstacles include generating a mesh that sufficiently represents the geometry of blood vessels and ensuring that this mesh is able to accurately resolve all the desired flow quantities.

Efficient and reliable computational methods are highly desirable to make blood flow simulations practically possible. In other words, an adaptive approach becomes valuable for simulating blood flow in the human arterial system. An adap-

tive procedure is designed to automatically control the accuracy of the numerical solution (or of any quantity of physical interest) in an efficient manner. Such an adaptive procedure will accelerate the convergence behavior leading to substantial savings in terms of computational resources. One way to automatically control the error in the numerical solution is to perform mesh adaptation based on *a posteriori* error estimators/indicators.

Mesh adaptation is achieved by modifying the mesh elements according to the size field information provided by the error estimator. Size field information given by scalar error estimates does not account for the directional features like boundary layers, shocks etc., that commonly arise in fluid flows. In other words, the available scalar error estimates lack the directional information required to construct an anisotropic size field to carry anisotropic mesh adaptation. However, desired mesh size in different directions, or mesh anisotropy, can be obtained by employing methods based on derivatives or second derivatives (Hessian) matrix of an appropriate solution variable. Anisotropic mesh adaptation procedures further reduce the number of elements (and degrees of freedom) leading to significant computational savings for a given level of accuracy.

1.2 Current Status

A common, and most importantly efficient, approach to control the error introduced due to discretization of the physical domain is to perform mesh adaptation that modifies the spatial discretization. One way to carry mesh adaptation is by applying local mesh modification procedures dictated by the size field information based on *a posteriori* error estimators/indicators. Traditionally, the size field is based on a scalar error information that allows for isotropic mesh adaptation resulting in, almost, equilateral elements.

Generally, the desired element size and orientation is significantly influenced by the characteristics of the solution field which in turn depend on the equations being solved, the initial and boundary conditions, and the geometry of the physical domain. Although equilateral elements would be good where the solution field is isotropic, in reality many physical problems exhibit strong anisotropic phenomena

that introduces a desire for anisotropic elements, for example, boundary layers that form near walls in viscous flows or shock waves in high speed flows. In this scenario, an anisotropic mesh adaptation procedure capable of creating such elements is highly desirable to further increase the efficiency of the simulations.

Recent efforts to obtain anisotropic meshes have considered the mesh metric field to define the required mesh anisotropy. A mesh metric field allows one to invoke local mesh modification operations (or perform remeshing process) in order to obtain elements that respect the required mesh anisotropy and in turn align the mesh with the solution anisotropy. Substantial progress has been made on the development of such procedures for three dimensional domain (see, [31] and references therein) including efforts on its application to a wide variety of physical problems in 2D ([2, 7, 8, 21]) and 3D ([15, 35, 38, 39]). Recently, such mesh modification procedures have also been extended to handle 3D curved geometries [32], which makes the process amenable to blood vessels.

Although anisotropic meshes have been used in the field of fluid mechanics for some time, especially for cases with a prior knowledge of boundary layers (see, for example [18, 24, 25, 27, 33] and literature cited therein), adaptive specification of the size field for 3D problems has been achieved only in the past few years [15, 35, 38, 39]. Most of the efforts carried out construct mesh metric field based on Hessian matrix of an appropriate solution variable.

The current status of blood flow simulation shows that mesh adaptation procedures have only recently been utilized (see, Prakash and Either [36]). All the attempts to improve the simulation efficiency of hemodynamics by means of mesh adaptivity are limited to isotropic adaptation over simple geometries and steady flows, while cardiovascular flows involve 3D complex geometries of blood vessels and are unsteady in nature. In this study, we have attempted to apply anisotropic mesh adaptation for pulsatile flows arising in the human arterial system over patient-specific geometries obtained from imaging data.

1.3 Our Approach

This study considers pulsatile flows arising in the cardiovascular systems over real blood vessel geometries. The inherent (quasi-) transient phenomena in blood flows complicate the process of mesh adaptation as the flow features can propagate and vary, in terms of shape and/or intensity, with time. There are two possible approaches to perform mesh adaptation for such problems. In the first, the mesh is continually adapted according to the transient flow features. The second approach is to use a single adapted mesh for the whole unsteady flow cycle. The latter approach is a practical alternative for flows of pulsatile nature and therefore periodic in time. The single mesh adaptation process for the whole flow cycle can be based on different scenarios of flow conditions like time averaged flow field, peak flow field over the cycle or spatially local peak flows. We propose a method in which the errors are identified by averaging the flow field over a cardiac cycle and then base the error analysis on this averaged flow field. In particular, we employ the Hessian strategy, discussed in section 3.2, by choosing the averaged flow speed as an appropriate solution variable.

1.4 Outline

The organization of the thesis is as follows. Chapter 2 introduces the numerical method that we use to solve hemodynamic flows along with a section that describes the computation of WSS, the most relevant physical quantity for blood flow simulations. Chapter 3 presents the overall anisotropic mesh adaptation procedure. In this chapter, we discuss the Hessian strategy and introduce the concept of a mesh metric field. We also present the details of anisotropic mesh size field computation. Chapter 4 considers the effects of mesh quality near the walls on WSS computation. In this chapter, we try to identify the mesh requirements in terms of element shape and gradation that will lead to more accurate prediction of WSS and also provide a possible methodology to meet the desired requirements. Chapter 5 demonstrates the applications of the anisotropic adaptive procedure for blood flows. We first demonstrate the efficiency of our procedure by applying it to a steady flow case in a straight cylindrical vessel. Here, we compare the computed

wall shear stress with the analytical values. We then increase the complexity of the problem by extending it to pulsatile flow for the same geometric model. The complexity is further increased by applying the method to steady flow in a blood vessel bifurcating into symmetric branches. Finally, we apply the procedure to a real case of porcine aorta with a stenosis bypassed by a graft for which experimental validation of the finite element method has been obtained by Ku *et al.* [28]. In this chapter, we also demonstrate the effect of element quality near the walls on WSS computation. Chapter 6 concludes the thesis by summarizing the results obtained and discussing future work.

CHAPTER 2
BLOOD FLOW SIMULATION

This chapter presents the finite element formulation for the transient incompressible Navier-Stokes equation governing blood flows. In this work, we use the stabilized finite element formulation that has been shown to be robust, accurate and stable on a variety of flow problems (see, for example, Jansen *et al.* [45] and Taylor *et al.* [43]). In particular, we employ the streamline upwind/Petrov-Galerkin (SUPG) stabilization method introduced by Brooks and Hughes [6].

The chapter also presents a discussion on the numerical computation of wall shear stress that plays a role of an important determinant in the formation of arterial diseases.

2.1 Governing Equations

The governing equations for blood flow, assuming Newtonian constitutive behavior and rigid blood vessel walls, are the transient incompressible Navier-Stokes equations:

$$u_{i,i} = 0, \tag{2.1}$$

$$\rho \dot{u}_i + \rho u_j u_{i,j} = -p_{,i} + \tau_{ij,j} + f_i. \tag{2.2}$$

The variables are: the velocity u_i, the pressure p, the density ρ, and the viscous stress tensor τ_{ij}. The summation convention is used throughout, i.e., sum on repeated indices. For incompressible flow the viscous stress tensor τ_{ij} is simply the symmetric strain rate tensor as shown below:

$$\tau_{ij} = \mu(u_{i,j} + u_{j,i}), \tag{2.3}$$

where, μ is the viscosity. Finally f_i is a body force or source term, such as gravity. This term is typically neglected in arterial flow analysis.

The above system of equations is supplemented with an appropriate set of boundary conditions that are prescribed on the model boundary of the blood vessels. The usual zero velocity, consistent with a no-slip condition is imposed on the rigid and impermeable vessel walls. A time varying velocity profile, based on the physiological values, is prescribed at the inlet. And a zero exit pressure in a weak sense is imposed at the traction-free outlet.

2.2 Flow Solver

Finite element methods are based on the weak form of the governing equations (2.1,2.2) which is obtained by taking the $L^2(\Omega)$-inner product of the entire system with weight functions. Integration by parts is then performed to move the spatial derivatives onto the weight functions. The diffusive term, pressure term and continuity equation are all integrated by parts. The diffusive term is integrated by parts to reduce continuity requirements, otherwise we would have second derivatives on our solution space. The pressure term is integrated by parts to provide symmetry with the continuity equation which in turn is integrated by parts to provide discrete conservation of mass. This process leads to an integral equation often referred to as the weak form.

To derive the finite element discretization from the weak form of the governing equations (2.1,2.2), discrete weight and solution function spaces must be introduced. Let $\bar{\Omega} \subset \mathbf{R}^N$ represent the closure of the physical spatial domain (i.e. $\Omega \cup \Gamma$ where Γ is the boundary) in N dimensions; where only $N = 3$ is considered here. The boundary is decomposed into portions with natural boundary conditions, Γ_h, and essential boundary conditions, Γ_g, i.e., $\Gamma = \Gamma_g \cup \Gamma_h$. In addition, $H^1(\Omega)$ represents the usual Sobolev space of functions with square-integrable values and derivatives on Ω. Subsequently Ω is discretized into n_{el} finite elements, $\bar{\Omega}_e$. With this, one can define the discrete solution and weight function spaces for the semi-discrete formulation as:

$$\boldsymbol{\mathcal{S}}_h^k = \{\boldsymbol{v}|\boldsymbol{v}(\cdot,t) \in H^1(\Omega)^N, t \in [0,T], \boldsymbol{v}|_{x\in\bar{\Omega}_e} \in P_k(\bar{\Omega}_e)^N, \boldsymbol{v}(\cdot,t) = \boldsymbol{g} \text{ on } \Gamma_g\}, \quad (2.4)$$

$$\boldsymbol{\mathcal{W}}_h^k = \{\boldsymbol{w}|\boldsymbol{w}(\cdot,t) \in H^1(\Omega)^N, t \in [0,T], \boldsymbol{w}|_{x\in\bar{\Omega}_e} \in P_k(\bar{\Omega}_e)^N, \boldsymbol{w}(\cdot,t) = \boldsymbol{0} \text{ on } \Gamma_g\}, \quad (2.5)$$

$$\mathcal{P}_h^k = \{p|p(\cdot,t) \in H^1(\Omega), t \in [0,T], p|_{x\in\bar{\Omega}_e} \in P_k(\bar{\Omega}_e)\}, \quad (2.6)$$

where, $P_k(\bar{\Omega}_e)$ is the space of all polynomials defined on $\bar{\Omega}_e$, complete up to order $k \geq 1$. Let us emphasize that the local approximation space, $P_k(\bar{\Omega}_e)$, is same for both the velocity and pressure variables. This is possible due to the stabilized nature of the formulation to be introduced below. These spaces represent discrete subspaces of the spaces in which the weak form is defined.

The stabilized formulation used in the present work is based on the formulation described by Taylor *et al.* [43]. Given the spaces defined above, the semi-discrete Galerkin finite element formulation is applied to the weak form of equations (2.1,2.2) as:

Find $\boldsymbol{u} \in \boldsymbol{\mathcal{S}}_h^k$ and $p \in \mathcal{P}_h^k$ such that

$$B_G(w_i, q; u_i, p) = 0, \quad (2.7)$$

$$\begin{aligned} B_G(w_i, q; u_i, p) = &\int_\Omega \{w_i\left(\rho\dot{u}_i + \rho u_j u_{i,j} - f_i\right) + w_{i,j}\left(-p\delta_{ij} + \tau_{ij}\right) - q_{,i}u_i\}\, d\Omega \\ &+ \int_{\Gamma_h} \{w_i\left(p\delta_{ij} - \tau_{ij}\right)n_j + q u_i n_i\}\, d\Gamma, \end{aligned} \quad (2.8)$$

for all $\boldsymbol{w} \in \boldsymbol{\mathcal{W}}_h^k$ and $q \in \mathcal{P}_h^k$. The boundary integral term arises from the integration by parts and is only carried out over the portion of the domain without essential boundary conditions.

Since the standard Galerkin method is well known to be unstable for equal-order interpolation of the velocity and pressure, additional stabilization terms are introduced as follows:

Find $\boldsymbol{u} \in \boldsymbol{\mathcal{S}}_h^k$ and $p \in \mathcal{P}_h^k$ such that,

$$B(w_i, q; u_i, p) = 0, \tag{2.9}$$

$$\begin{aligned} B(w_i, q; u_i, p) = {} & B_G(w_i, q; u_i, p) \\ & + \sum_{e=1}^{n_{el}} \int_{\bar{\Omega}_e} \{\tau_M (u_j w_{i,j} + q_{,i}/\rho)\mathcal{L}_i + \tau_C w_{i,i} u_{j,j}\}\, d\Omega_e \\ & + \sum_{e=1}^{n_{el}} \int_{\bar{\Omega}_e} \{w_i \rho \overset{\Delta}{u}_j u_{i,j} + \hat{\tau}\mathcal{L}_j w_{i,j} \mathcal{L}_k u_{i,k}\}\, d\Omega_e, \end{aligned} \tag{2.10}$$

for all $\boldsymbol{w} \in \boldsymbol{\mathcal{W}}_h^k$ and $q \in \mathcal{P}_h^k$. We have used $\mathcal{L}_i$ to represent the residual of the i^{th} momentum equation,

$$\mathcal{L}_i = \rho \dot{u}_i + \rho u_j u_{i,j} + p_{,i} - \tau_{ij,j} - f_i. \tag{2.11}$$

The second line in the stabilized formulation, (2.10), represents the typical SUPG stabilization added to the Galerkin formulation for the incompressible set of equations (see Franca and Frey [13]). The first term in the third line of (2.10) was introduced by Taylor *et al.* [43] to overcome the lack of mass conservation introduced as a consequence of the momentum stabilization in the continuity equation. The second term on this line was introduced to stabilize this new advective term.

The stabilization parameters for continuity and momentum equations are defined as:

$$\tau_M = \frac{1}{\sqrt{2c_1/{\Delta_t}^2 + u_i g_{ij} u_j + c_2 \nu^2 g_{ij} g_{ij}}}, \tag{2.12}$$

$$\tau_C = \frac{\rho}{8\tau_M \mathrm{tr}(g_{ij})}, \tag{2.13}$$

and the stabilization of the new advective term is defined in direct analogy with the advective portion of τ_M as:

$$\hat{\tau} = \frac{\tau_M}{\sqrt{\mathcal{L}_i g_{ij} \mathcal{L}_j}}, \tag{2.14}$$

with

$$\overset{\Delta}{u}_i = -\tau_M \mathcal{L}_i / \rho, \tag{2.15}$$

where, c_1 and c_2 are defined based on considerations of the one-dimensional, linear advection-diffusion equation using a linear finite element basis and $g_{ij} = \xi_{k,i}\xi_{k,j}$ is the covariant metric tensor related to the mapping from global to element coordinates. It should be noted that for tetrahedral elements, this mapping depends on the orientation of the element, and therefore must be corrected to create an invariant element length-scale by permuting the possible choices of orientation. This term may be identified with the element length-scale, and is hence a mesh dependent parameter.

To summarize, we use the SUPG stabilized formulation for the transient incompressible Navier-Stokes equations, governing blood flow, that are discretized by linear finite elements, both for the pressure and the velocity field. Now, to develop a discrete system of algebraic equations, the weight functions w_i and q, the solution variables u_i and p, and their time derivatives are expanded in terms of the finite element basis functions. Gauss quadrature of the spatial integrals results in a system of first-order, nonlinear differential-algebraic equations. Finally this system of non-linear ordinary differential equations is discretized in time via a generalized-α time integrator (see Jansen *et al.* [26]) resulting in a non-linear system of algebraic equations. This system is in turn linearized with Newton's method which yields a linear algebraic system of equations that is solved (at each time step) and the solution is updated for each of the Newton iterations. The linear algebra solver of Shakib [40] is used to solve the linear system of equations.

2.3 Wall Shear Stress Computation

Wall shear stress (WSS) can be defined via the surface traction vector $\boldsymbol{t}$ whose components are given as:

$$t_i = (-p\delta_{ij} + \tau_{ij})\, n_j, \tag{2.16}$$

p denoting the pressure, τ_{ij} are the components of the viscous stress tensor and n_j are the components of the normal $\boldsymbol{n}$ to the surface. The WSS is then defined, on each point on the surface, as:

$$t_w = |\boldsymbol{t}_w| = |\boldsymbol{t} - (\boldsymbol{t} \cdot \boldsymbol{n})\boldsymbol{n}|, \tag{2.17}$$

that is, the magnitude of the traction vector's component in the plane of the surface.

Traditionally the boundary quantities also referred as wall quantities, like the viscous fluxes $\hat{\tau}_{in}$ $(= \tau_{ij} n_j)$, are evaluated by substituting the numerical derivatives of flow quantities into the definition of the fluxes. However, instead of computing the viscous flux in a usual way (i.e., by differentiating the velocity) one can introduce a modified finite element formulation with an auxiliary flux field which amounts for the boundary flux, i.e., on the portion with essential boundary conditions, Γ_g (see, Hughes [22, page 107] , Hughes *et al.* [23]). Taking $\hat{\tau}_{in}$, as the unknown (discrete) viscous flux, the modified formulation which derives from the discrete weak formulation (2.10) is:

Find $\boldsymbol{u} \in \boldsymbol{\mathcal{S}}_h^k$, $p \in \mathcal{P}_h^k$ and $\hat{\tau}_{in} \in \boldsymbol{W}_h^k - \boldsymbol{\mathcal{W}}_h^k$ such that,

$$B_{mod}(w_i, q; u_i, p) = 0, \tag{2.18}$$

$$\begin{aligned} B_{mod}(w_i, q; u_i, p) &= B(w_i, q; u_i, p) \\ &\quad + \int_{\Gamma_g} \hat{w}_i(-\hat{\tau}_{in})\, d\Gamma \qquad \forall \hat{\boldsymbol{w}} \in \boldsymbol{W}_h^k - \boldsymbol{\mathcal{W}}_h^k. \end{aligned} \tag{2.19}$$

Note that the above problem splits into two subproblems:

$$B(w_i, q; u_i, p) = 0 \qquad \forall \boldsymbol{w} \in \boldsymbol{\mathcal{W}}_h^k, \tag{2.20}$$

$$\int_{\Gamma_g} \hat{w}_i \hat{\tau}_{in}\, d\Gamma = B(\hat{w}_i, q; u_i, p) \qquad \forall \hat{\boldsymbol{w}} \in \boldsymbol{W}_h^k - \boldsymbol{\mathcal{W}}_h^k, \tag{2.21}$$

where, $\boldsymbol{W}_h^k$ is the discrete function space spanned by the basis functions; including the ones omitted to satisfy the homogenous essential boundary conditions. Let η denote the set of all degrees of freedom (*dof*) and η_g be the subset corresponding to the ones located on Γ_g. $\boldsymbol{\mathcal{W}}_h^k$ spans all the basis functions associated with $\eta - \eta_g$, as:

$$\boldsymbol{\mathcal{W}}_h^k = span\{\boldsymbol{N}_A\}_{A \in \eta - \eta_g}, \tag{2.22}$$

where, $\boldsymbol{N}_A$ is basis function associated with *dof* $\boldsymbol{d}_A$. Now, $\boldsymbol{W}_h^k$ can be expressed as:

$$\boldsymbol{W}_h^k = \boldsymbol{\mathcal{W}}_h^k \bigoplus span\{\boldsymbol{N}_A\}_{A \in \eta_g}. \tag{2.23}$$

This technique is often referred as the *consistent* boundary-flux calculation technique and it is constructed to satisfy the conservation properties, see, e.g., Gresho and Sani [20, pages 42–44] and Hughes *et al.* [23]. The auxiliary problem (2.21) is solved for the boundary flux after the original problem (2.20) as a post-processing step (i.e., if $\boldsymbol{u}$ ($\in \boldsymbol{\mathcal{S}}_h^k$) is already determined by (2.20), then the right-hand side of (2.21) is completely determined). The flux is expressed in terms of the basis functions associated with η_g. The integrals in (2.21) exist only over the elements touching Γ_g, due to the compact support of basis functions, making the auxiliary problem inexpensive.

The traction vector, $\boldsymbol{t}$, can be computed once $\hat{\tau}_{in}$ is known, which in turn can be used to compute the WSS magnitude as defined in (2.17). The remaining step is the computation of the normal, $\boldsymbol{n}$, at boundary nodes. Noting the normal is poorly defined at nodes on curved boundaries (i.e., vessel walls) because of the C^0 elements, the final task is to find an appropriate normal. In this work, we use basis function weighted normals as described in Gresho and Sani [20, pages 542–544].

CHAPTER 3
ANISOTROPIC ADAPTIVE PROCEDURE

The accuracy of the numerical solution significantly depends on the spatial discretization of the physical domain, i.e., on the process of subdividing the domain into finite number of elements. In general, the desired element size in different directions are influenced by the physical and geometric features of the problem that varies significantly over the domain. In many physical problems, including blood flows, the solution exhibits strong anisotropic features that generates a need for elements which are aligned with the solution anisotropy. Unfortunately, for real cases such information, required to compute the desired solution field to an acceptable level of accuracy, is unknown *a priori*.

An efficient approach to overcome this difficulty is to apply an adaptive procedure where the errors introduced due to spatial discretization are controlled within a specified tolerance. The goal of such an adaptive scheme is to modify the spatial discretization so that the errors are controlled effectively. An anisotropic adaptive procedure modifies the spatial discretization in a way such that it is adequate in all directions.

In this chapter, we describe the anisotropic adaptive procedure employed in this work. We describe the basis for Hessian strategy and introduce the concept of mesh metric tensors that is used to represent the desired mesh anisotropy. The last section of this chapter presents the details of the anisotropic mesh size field computation.

3.1 General Components

An adaptive method involves a feed-back process that evaluates the quality of the computed solution in order to efficiently control the error(s). It typically involves a stopping criterion to control the error within a user specified tolerance, which if not satisfied invokes a modification strategy. For real applications both of these items are based on *a posteriori* error information.

In order to control the errors introduced due to spatial discretization, referred as *discretization* error, the mesh modification procedures change the local mesh resolution. It is well known, for consistent numerical methods, that increased mesh resolution leads to more accurate solutions. The rate at which the error is reduced as the element size is reduced governs the convergence behavior of the process. The goal of an adaptive meshing technique is to accelerate this convergence rate in an *optimal* fashion, which can be possibly achieved through equidistribution of the errors iteratively [42]. Such techniques have found its use in applications as diverse as solid mechanics, fluid mechanics, geomehanics, electromagnetics, semi-conductor device simulations, and image processing, among many others.

The key ingredients of an adaptive meshing method include:

- *A posteriori* error estimation/indication: estimating and/or obtaining an indication of the discretization error based on the quality of the computed solution. See, Ainsworth and Oden [1] or Verfürth [44] for a survey.

- Size field construction: this step involves the transformation of the error information into a size field information that describes the desired mesh resolution over the domain. This can be achieved by equidistribution of the local errors over the domain.

- Modifying strategy: the last ingredient involves modification of the mesh elements based on the size field information. This strategy can be applied based on local mesh modifications [4, 11] or global remeshing [19].

The above components are general enough to include anisotropic mesh adaptation techniques provided each one of them incorporate appropriate directional information. The remainder of this chapter elaborates on each of these key components, except the last one that has been described in [30, 31], for anisotropic adaptive procedures.

3.2 Hessian Strategy

To extract directional information of the error we use the Hessian strategy [29], a method where the field's second derivatives are used to obtain information on the

error distribution. This directional information can be in turn converted into a mesh metric field (discussed in the next section) which prescribes the desired element size and orientation.

To illustrate the origin of the discretization error, we recall that a function which is sufficiently smooth can be developed into a Taylor series as:

$$u(x) = u(\bar{x}) + h \left.\frac{du}{dx}\right|_{\bar{x}} + \frac{1}{2}h^2 \left.\frac{d^2u}{dx^2}\right|_{\bar{x}} + O(h^3). \tag{3.1}$$

When trying to interpolate that function with a piecewise linear function, the interpolation error will have a lowest order error term (i.e., second order) proportional to the second derivatives of the function. Therefore, the interpolation error is equivalent to second derivatives for linear finite elements and a large portion of the discretization error is covered by this error [9].

For the sake of simplicity, we show this for a one-dimensional case and then generalize it for a three-dimensional case. Let u be approximated by u^h as piecewise linear interpolation (see Fig. 3.1) then the local interpolation error $e_I = u_I - u_I^h$ is bounded over an interval I as follows [10]:

$$|e_I| \leq c_1 h_I^2 \max_{\bar{x}\in I} \left|\frac{d^2 f}{dx^2}(\bar{x})\right|, \tag{3.2}$$

where, c_1 is a constant and h_I is the interval length.

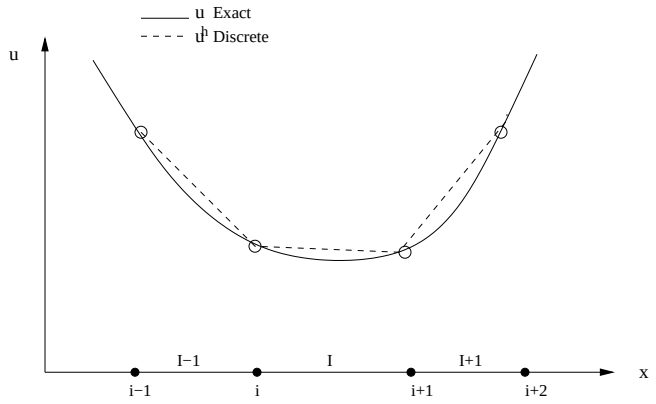

Figure 3.1: Linear approximate solution

In this way, the generalization of the interpolation error for 3D in the L_∞ norm defined on an element K can be measured as follows [14]:

$$\|e_K\|_{\infty,K} \leq c_1 \max_{x \in K} \max_{\boldsymbol{v} \subset K} \langle \boldsymbol{v}, |H(x)| \boldsymbol{v} \rangle, \tag{3.3}$$

$$\leq c_1 \max_{x \in K} \max_{\boldsymbol{e} \in E_K} \langle \boldsymbol{e}, |H(x)| \boldsymbol{e} \rangle, \tag{3.4}$$

where, c_1 is a constant independent of element parameters, $\boldsymbol{v}$ is any vector contained in the element, E_K is the set of element edges and $|H|$ is the absolute value of the Hessian matrix of the solution (i.e., consists of absolute eigenvalues). To obtain such error estimates over the domain in different norms see references [3, 12, 29]. Note that the Hessian strategy is based on certain assumptions on regularity of the solution and interpolation estimates, see Kunert [29].

The Hessian strategy involves the computation of the matrix of second derivatives. As the Hessian matrix is symmetric, it can be decomposed as:

$$H = \mathcal{R} \Lambda \mathcal{R}^T, \tag{3.5}$$

where, $\mathcal{R}$ is the eigenvector matrix and $\Lambda = diag(\lambda_k)$ is the diagonal matrix of eigenvalues ($k = 1, 2, 3$ in 3D). The strategy is based on the idea that a high magnitude of eigenvalue implies high error in the direction associated with the corresponding eigenvector, so a small element size would be desired in this direction. Conversely, low magnitude of eigenvalue in a particular eigendirection suggests that the element size can be large in this direction. This is discussed further in the section 4 of this chapter.

3.3 Mesh Metric Field

To perform anisotropic mesh adaptation requires a way to define the desired element size distribution over the domain. Mesh metric tensors are used to represent an anisotropic mesh size field defining the desired mesh anisotropy at a point (see, for example, [5]). The concept of a mesh metric field is used to represent the desired size field as a tensor over the domain.

The mesh metric tensor at any point P in the domain is defined as a symmetric positive definite matrix $\mathcal{M}$. The associated quadratic form $\langle \boldsymbol{x}, \mathcal{M} \boldsymbol{x} \rangle = 1$, whose ge-

ometric representation will be an ellipsoidal surface (see Fig. 3.2), defines a mapping of an ellipsoid in the physical space into a unit sphere in the *transformed/metric* space. In other words, any vector $\boldsymbol{x}$ at point P assumes a unit value in the space where distances are measured under the metric $\mathcal{M}$.

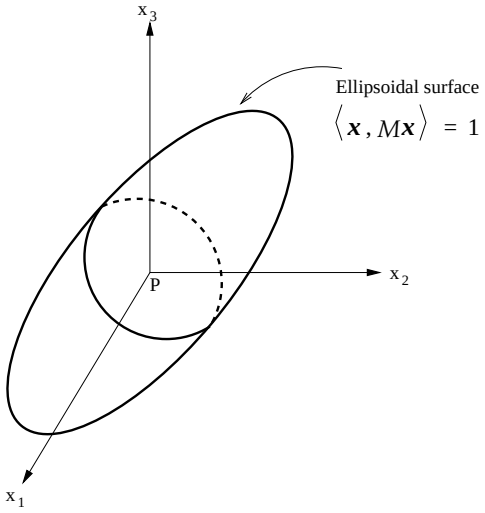

Figure 3.2: Ellipsoidal surface associated with the quadratic form

The ideal goal of the mesh adaptation algorithm is to yield a mesh with regular elements in the metric space where each edge $\boldsymbol{e}$ must satisfy the following equality:

$$\langle \boldsymbol{e}, \mathcal{M}\boldsymbol{e} \rangle = 1. \tag{3.6}$$

A mesh with all its edges satisfying the above relationship is commonly referred as a *unit mesh*. However, the fact that we cannot pack unit regular tetrahedra to satisfy a constant unit mesh metric field over a domain indicates that a perfect match is not possible. Therefore, using a relaxed criteria is inevitable. For further details on issues of relaxed criteria for mesh modifications and element quality measures in the transformed space see references [30, 31]. The same reference also provides the details of discretization of mesh metric field over the domain along with its implementation.

3.4 Size Field Computation

In this study, we carry out anisotropic mesh adaptation dictated by a local directional error indicator based on the second derivatives of the finite element solution. The crucial step is the construction of a size field, which represents the desired solution characteristics, that can be fed to the mesh adaptation module. The key point in the construction of a size field is equidistribution of the error in all directions.

The interpolation errors for piecewise linear approximation are represented by the second derivatives (Hessian) matrix which is given by:

$$H = \begin{pmatrix} \frac{\partial^2 u}{\partial x^2} & \frac{\partial^2 u}{\partial x \partial y} & \frac{\partial^2 u}{\partial x \partial z} \\ \frac{\partial^2 u}{\partial y \partial x} & \frac{\partial^2 u}{\partial y^2} & \frac{\partial^2 u}{\partial y \partial z} \\ \frac{\partial^2 u}{\partial z \partial x} & \frac{\partial^2 u}{\partial z \partial y} & \frac{\partial^2 u}{\partial z^2} \end{pmatrix}. \tag{3.7}$$

This is a real symmetric matrix that can be decomposed into real eigenvalues λ_k and corresponding orthogonal eigenvectors $\boldsymbol{p}_k$, for $k = 1, 2, 3$ in 3D. The directions associated with the eigenvectors are referred as principal directions. The eigenvalues are then equivalent to the second derivatives along the local principal directions.

Provided the exact solution is known, it is then possible to estimate the error in an element from the interpolation error equation (3.4). To achieve a suitable mesh resolution in different directions, a uniform distribution of local errors is applied in the principal directions which leads to:

$$h^2_{\boldsymbol{p}_k} |\lambda_k| = \epsilon, \qquad (k = 1, 2, 3), \tag{3.8}$$

where, ϵ is the user specified tolerance on error. In this way, a mesh metric tensor can be constructed by scaling the Hessian (or its eigenvalues) with the aim of reaching the specified error level through equidistribution of error in all directions. In other words, we want to modify the mesh size, in terms of edge lengths, such that the error in any direction reaches the specified level.

Practically the exact solution is not known and therefore, it creates a need for an approximation of the Hessian matrix to estimate the interpolation error. To do this we reconstruct the second derivatives at each node based on the computed

solution (described later). With the help of reconstructed Hessian matrix at nodes we obtain an estimate of the interpolation error over each edge of a node through inner product as follows:

$$e_i^{j_i} = \langle \boldsymbol{e}_{j_i}, |H|_i^R \boldsymbol{e}_{j_i} \rangle, \tag{3.9}$$

where, i is the node number, $\boldsymbol{e}_{j_i}$ is the j^{th} edge around node i and H_i^R is the reconstructed Hessian matrix at node i. This process is shown at node i for a 2D case in Fig. 3.3.

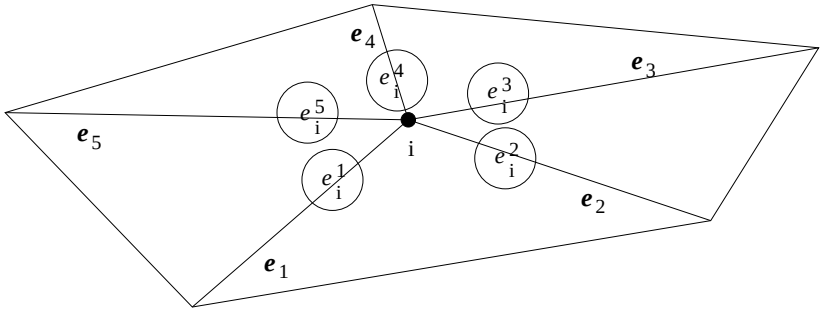

Figure 3.3: Error estimates ($e_i^{j_i}$) over edges ($\boldsymbol{e}_{j_i}$) of node i in a 2D case

The leading error term among these error estimates over edges at node i is taken as an indicator of the error ei_i at that node:

$$ei_i = \max_{j_i \in E_i} e_i^{j_i}, \tag{3.10}$$

where, E_i is the set of edges around node i. As we obtain an indication of the error the user is asked to specify a reduction factor, γ, to define the desired error level $\tilde{\epsilon}$. The desired error level is then determined based on the user specified reduction factor and the mean of the leading error terms over the nodes as follows:

$$\tilde{\epsilon} = \gamma \frac{1}{N} \sum_{i=1}^{N} ei_i, \tag{3.11}$$

where, N is the total number of nodes.

Now, to recover the second derivatives at a node we employ a reconstruction

technique, among many possibilities, that uses the derivative information from the patch S_i of all elements K surrounding that node. In the first step we recover the gradient of an approximate field component u^h at node i as follows:

$$\nabla^R(u^h)_i = \frac{1}{|S_i|} \sum_{K \in S_i} |K| \nabla(u^h|_K), \tag{3.12}$$

where, $|K|$ and $|S_i|$ are the volume of element K and the patch of elements S_i around node i. This is equivalent to a lumped-mass approximation by least squares reconstruction of the gradient for linear elements. A schematic for such a recovery technique is shown in Fig. 3.4.

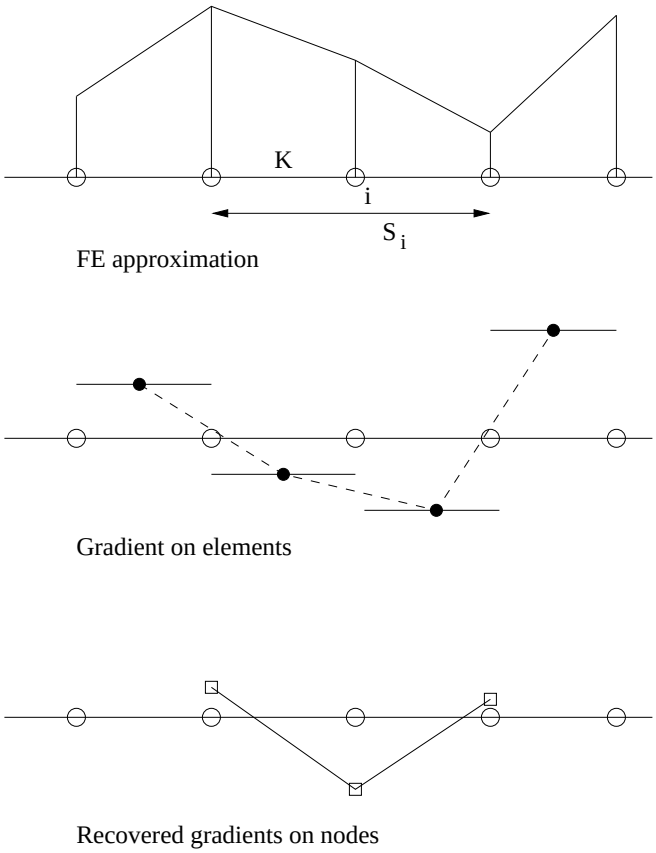

Figure 3.4: Schematic of gradient recovery technique in 1D

The same procedure applied to each term of second derivatives yields the reconstructed Hessian matrix. We should note that values that are reconstructed on the domain boundary in this way usually does not very well represent the actual

Hessian, therefore a simple extrapolation technique is applied to project the interior values onto the nodes that lie on the domain boundary. In this technique, for current applications, the mean of values at interior nodes around a boundary node is assumed at that boundary node for each component of the Hessian.

A mesh metric tensor is then obtained at each node by calculating a scaled eigenspace of the recovered Hessian matrix as:

$$\overline{\mathcal{M}} = \mathcal{R}\bar{\Lambda}\mathcal{R}^T, \tag{3.13}$$

where, $\mathcal{R}$ is the eigenvector matrix and $\bar{\Lambda} = \Lambda/\tilde{\epsilon}$ is the diagonal matrix of scaled eigenvalues. $\mathcal{R}$ and Λ are defined in eq. (3.5) whereas $\tilde{\epsilon}$ is defined in eq. (3.11) and is used to scale the eigenvalues at each node.

Truncation values h_{min} and h_{max} for mesh size are specified to limit the eigenvalues. One reason for truncating the element size, in terms of edge length, is to avoid singular metrics. For example, it is necessary to apply h_{max} in case eigenvalue is zero (or close to zero) in the direction where the solution does not vary. The modified eigenvalues of the Hessian matrix then becomes:

$$\tilde{\lambda}_k = \min(\max(\tilde{\epsilon}^{-1}|\lambda_k|, \frac{1}{h_{max}^2}), \frac{1}{h_{min}^2}), \qquad (k = 1, 2, 3). \tag{3.14}$$

The final mesh metric field is then constructed at each node through multiplication of the diagonal matrix of modified eigenvalues $\tilde{\Lambda} = diag(\tilde{\lambda}_k)$ with the matrix $\mathcal{R}$ of eigenvectors, as shown below:

$$\mathcal{M} = \mathcal{R}\tilde{\Lambda}\mathcal{R}^T. \tag{3.15}$$

CHAPTER 4
CONTROLLING MESH ADAPTATION

In this chapter, we assess the accuracy of the numerical results obtained on adapted meshes and identify the mesh requirements that must be met by the adaptive procedures to improve the reliability of the computation. We also introduce a possible methodology that enables adaptive procedures to meet the desired mesh requirements. The assessment is based on preliminary viscous flow simulations performed for two cases. One being a high shear flow between parallel plates and other with the identical inflow profile in a straight pipe.

With this goal we first determine the sensitivity of viscous flux predictions, namely wall shear stress (WSS), to mesh quality close to the walls. We then try to identify the mesh requirements in order to improve the accuracy of the computed quantities like WSS. In this way, the investigation is performed in order to define the objectives for adaptive procedures that can produce suitable meshes for accurate prediction of boundary or wall quantities.

4.1 Mesh Requirements for Viscous Flows

Adaptive procedures based on strategies as given in chapter 3 have proved to be successful in automatically obtaining highly anisotropic meshes aligned with the solution anisotropy for 3D problems, see the results presented in section 5.1. Although the capabilities of the adaptive procedures have been clearly demonstrated, improved procedures are required to obtain better accuracy in the prediction of wall quantities, like WSS. In section 5.2 this is shown for two examples, where we observe that the predicted WSS values are better on meshes which have structured layer(s) of elements close to the walls.

Moreover, turbulence models, like Spalart-Allmaras one-equation turbulence model [41], are also highly sensitive to the mesh quality near the walls. We have observed that to correctly predict the near wall behavior of the turbulent scalar variable require many structured layers of elements close to the walls. This requires

further careful investigations and is considered to be a topic of future research.

See, for example [16, 24, 27], where the predictions of wall quantities, like pressure distributions and skin friction coefficients, on meshes with structured elements close to the walls have been shown to be in excellent agreement with the experimental ones for complex aerospace geometries. The meshes used in therein involved user intervention in the sense that they were generated based on a prior knowledge of the flow features.

Mesh generation for such viscous flow simulations have been tackled and addressed by many researchers (see, [18] and references therein). The main idea of the technique, referred as *generalized advancing layer method*, is to inflate the surface mesh into the volume along the local surface normals. The inflation process is generalized by making it flexible to be able to handle geometries with sharp corners or edges. Such a mesh possesses structure in the direction normal to the walls by creating highly anisotropic triangular prisms and is called a boundary layer (BL) mesh. A schematic of boundary layer elements is shown in Fig. 4.1.

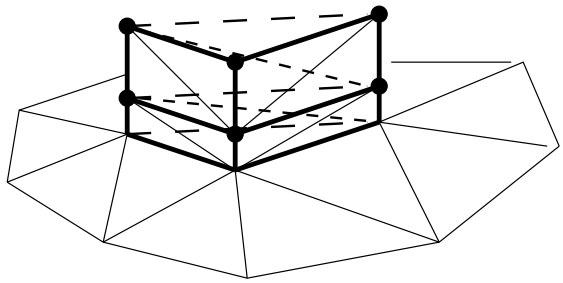

Figure 4.1: A schematic of boundary layer elements: triangular prisms are tetrahedronized.

Generally, flow features arising in real applications are unknown *a priori* therefore adaptive procedures are needed to accurately resolve them. Although adaptive procedures governed by the mesh metric field helps to produce highly anisotropic meshes with the help of general mesh modification procedures, special treatment of elements close to the walls appears to be necessary to introduce and/or maintain structured layers as generated in a boundary layer mesh very near the walls. In

this study, we describe preliminary steps for adaptive procedures that can maintain structured layers of elements close to the walls.

4.2 Control of Mesh Adaptation

In this section, we describe a possible methodology that enables adaptive procedures to maintain structured and graded elements near the walls for accurate prediction of wall quantities. The idea is to consider BL elements as a product of a surface mesh (2D) and a thickness mesh (1D) as depicted in Fig. 4.2. To preserve the structure of the mesh along the normals of the walls the adaptive procedure can be divided into two steps: surface adaptation and thickness modification. To perform surface adaptation mesh modifications can be carried on the surface mesh while layer thickness can be changed by applying modifications in the thickness mesh.

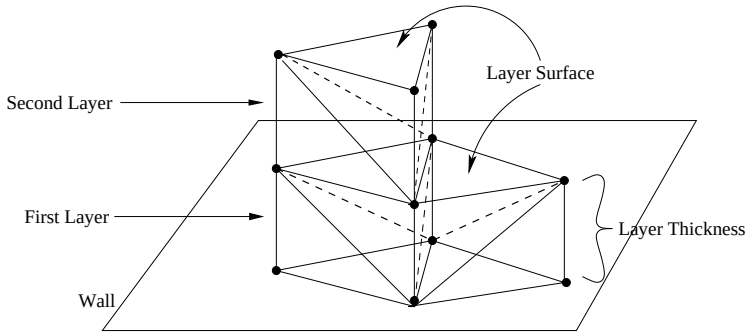

Figure 4.2: Conceptual decomposition of a boundary layer element.

This two step adaptive procedure can be dictated by the mesh metric field. The mesh metric field at any point can also be decomposed into a component on the layer surface and a normal component along the layer thickness, see Fig. 4.3. As described in chapter 3, a mesh metric tensor $\mathcal{M}$ at any node in a 3D case consists of three eigenvalues and corresponding principal directions. The planar part (see Fig. 4.3) of a mesh metric tensor can be defined on the basis of the projection of two principal directions on the layer surface.

One of the principal directions will be more aligned to the local surface normal

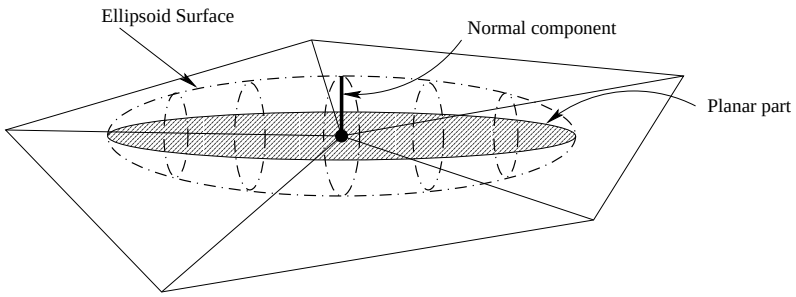

Figure 4.3: Conceptual decomposition of a mesh metric tensor.

vector $\boldsymbol{n}$ than the other two (for regions with boundary layers only, i.e., without shocks and corners, it will be associated with the largest eigenvalue and will be totally aligned with the normal vector ideally). The plane containing the other two principal directions will be the one closer to the layer surface. Now, the principal direction associated with the largest eigenvalue among the ones associated with the remaining two principal directions, referred as $\bar{\boldsymbol{v}}$, can be projected on the layer surface (see Fig. 4.4) as follows:

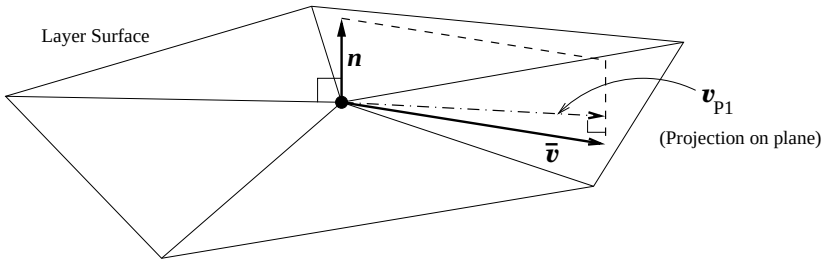

Figure 4.4: Projection of a principal direction on layer surface.

$$\boldsymbol{v}_{P1} = \bar{\boldsymbol{v}} - (\bar{\boldsymbol{v}} \cdot \boldsymbol{n})\boldsymbol{n}, \tag{4.1}$$

where, $\boldsymbol{v}_{P1}$ is the projection of $\bar{\boldsymbol{v}}$ on the layer surface. Here, we essentially remove the part of the vector along the surface normal $\boldsymbol{n}$. The second direction on the plane of the layer surface that is orthogonal to $\boldsymbol{n}$ and $\boldsymbol{v}_{P1}$ will be:

$$\boldsymbol{v}_{P2} = \boldsymbol{n} \times \bar{\boldsymbol{v}}. \tag{4.2}$$

The choice of largest eigenvalue among the ones associated with the two principal directions closer to layer surface will ensure for attainment of error within desired level. The mesh size along any of the projected vectors will be: $h_{Pk} = \boldsymbol{v}_{Pk}\mathcal{M}\boldsymbol{v}_{Pk}^T$ (for $k = 1, 2$). The planar part of a mesh metric tensor can then be determined based on the two projected principal directions $\boldsymbol{v}_{Pk}$ and sizes along these directions h_{Pk}. Similarly, the normal component of the mesh metric tensor can be computed as: $h_n = \boldsymbol{n}\mathcal{M}\boldsymbol{n}^T$.

With this information at hand, the decision to apply any mesh modification procedure on a layer's surface will be based on the planar part of the mesh metric tensor and any change in the layer thickness will be based on the normal component. Basic mesh modification operations, like edge split, edge collapse, node movement etc. [11, 31], can be applied to perform these steps.

The edges of a boundary layer element can be classified into three categories, as depicted in Fig. 4.5:

- *Layer edge* : All the edges of a BL element that have their nodes on the same layer surface.
- *Growth edge* : Shortest edge, along the surface normal, of a BL element that has its nodes on different layer surfaces.
- *Diagonal edge* : All the remaining edges of a BL element (that essentially tetrahedronize the BL prisms).

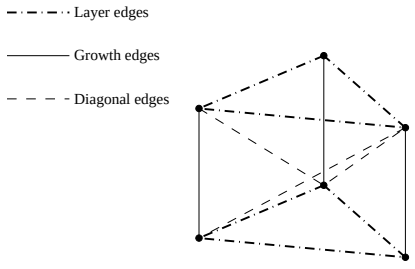

Figure 4.5: Classification of edges of a boundary layer element.

To perform adaptation on a layer surface only *layer edges* will take part in the modification process whereas to change the thickness of layers only *growth edges* will be split (or collapsed) and/or their length will be adjusted through node movement. The existence of *diagonal edges* (see, Fig. 4.5) makes the process tedious, but considering the inherent structure of triangular prisms allows one to simplify the process.

The surface adaptation is possible with the help of three basic mesh modification operations:

1. **Edge Split** : An edge split operation will split a *layer edge* into two *layer edges*. See Fig. 4.6 to see the initial and final mesh topology.

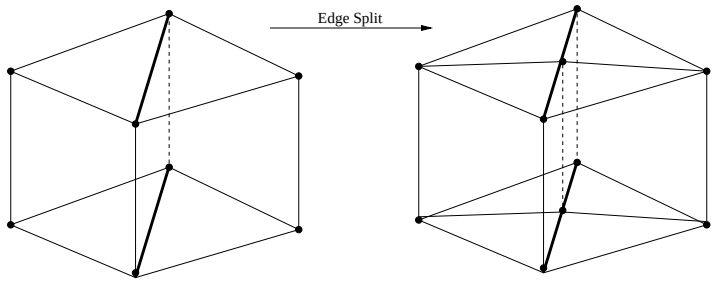

Figure 4.6: Mesh topology before (left) and after (right) edge split

2. **Edge Collapse** : An edge collapse operation will collapse a *layer edge*. See Fig. 4.7 to see the initial and final mesh topology.

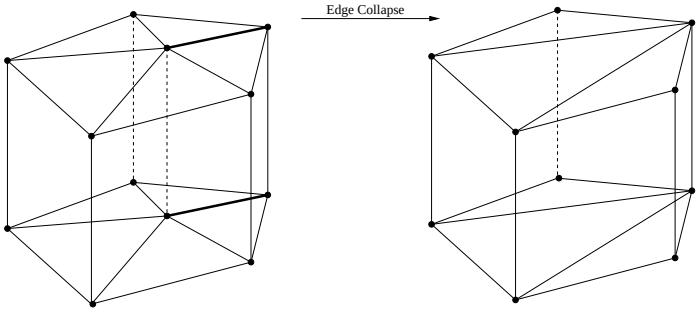

Figure 4.7: Mesh topology before (left) and after (right) edge collapse

3. **Edge Swap** : An edge swap operation will swap a *layer edge*. See Fig. 4.8 to see the initial and final mesh topology.

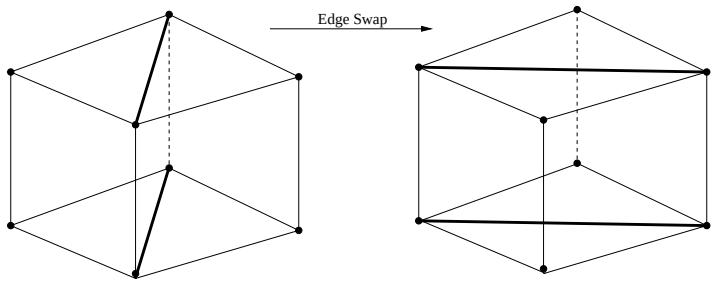

Figure 4.8: Mesh topology before (left) and after (right) edge swap

In all the operations, basic geometric and topological validity checks must be done (see appendix A in [17] for details). For surface adaptation, these will be performed to check the validity only on the layer's surface as depicted in Fig. 4.9.

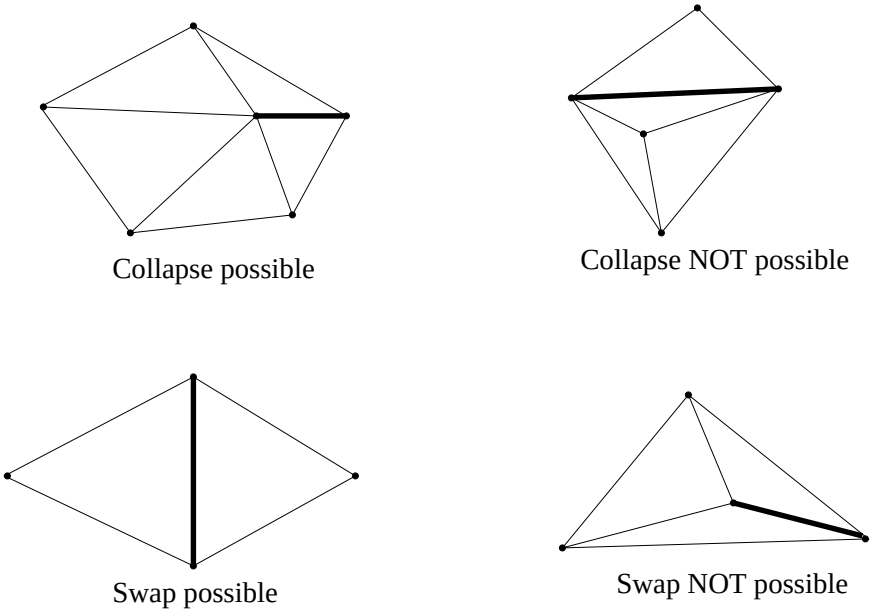

Figure 4.9: Validity checks on layer's surface

To change the thickness of the layers basic operations of edge split and/or node movement can be performed. It is possible to carry both of these operations in a way that results in graded elements in the normal direction. For example, in the process of edge split operation the position of the newly created node can be determined on the basis of the ratio of the normal component of the two mesh metric tensors at the two end nodes of the *growth edge*. Node movement can be also applied in the normal direction to obtain smooth transition in element lengths.

With the idea of working with triangular BL prisms, a mesh modification operations can be carried out on a single layer's surface and propagated through all the layers as shown in Fig 4.10(a). Node movement can be applied to change the layer thickness while maintaining the number and topology of layers. To introduce more structured layers of elements *growth edges* can be subdivided to create new nodes and in turn layers, see Fig. 4.10(b). After carrying out all the mesh modification operations each of the boundary layer prisms can be tetrahedronized (see [18] for tetrahedronization of triangular prisms). Extension of procedures changing the number of layers to handle complex geometries with sharp corners or edges where the boundary layers have topological adjustments in them will require some additional considerations.

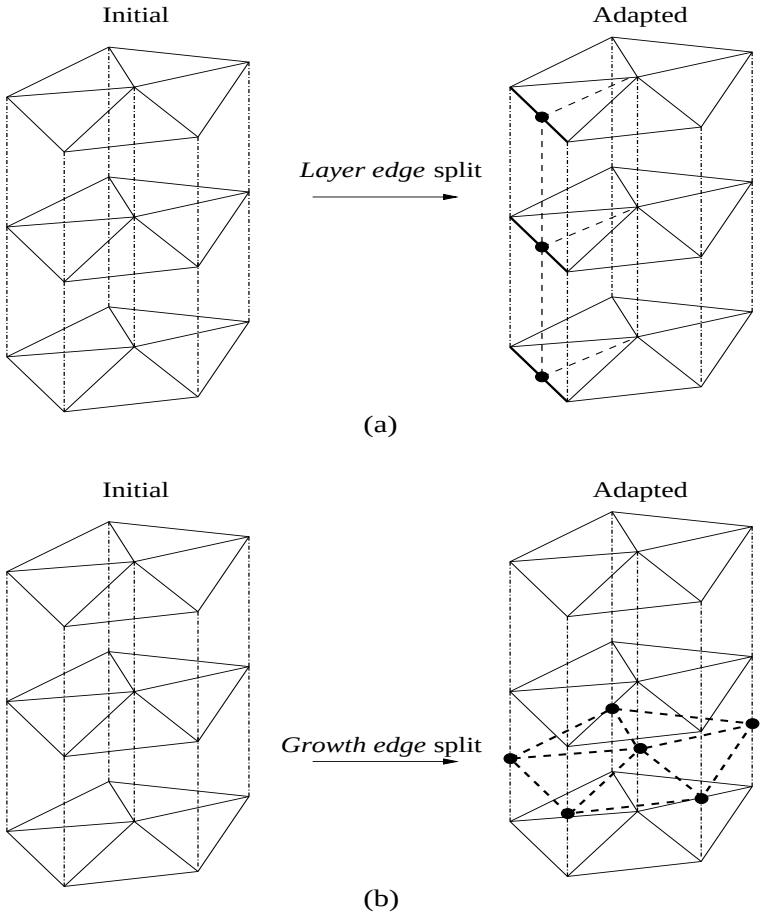

Figure 4.10: Mesh modification applied on boundary layer prisms.

CHAPTER 5
APPLICATION TO BLOOD FLOWS

In this chapter, we present the results obtained in the current work to demonstrate the efficiency of our method. This chapter has been divided into two sections. The first section presents the results for cases in which we apply anisotropic adaptive procedures presented in chapter 3. The second section investigates the effect of mesh quality close to the vessel walls in wall shear stress (WSS) computation.

We first apply our method to steady flow in a straight cylindrical blood vessel. We then increase the complexity of the problem by extending it to pulsatile flow for the same geometric model. The complexity is further increased by applying the method to steady flow in a blood vessel with a symmetric bifurcation. Finally, we apply the procedure to a real case of porcine aorta with a stenosis bypassed by a graft for which experimental validation of the finite element method has been obtained by Ku *et al.* [28].

The second section of the chapter presents results for steady turbulent flow in a channel and straight pipe. In this part we compare the WSS values obtained on an adapted mesh to the ones where elements close to vessel walls are structured in the direction normal to the walls.

5.1 General Mesh Adaptation

5.1.1 Straight Cylindrical Vessel

In this case we compute the flow in a blood vessel as depicted in Fig. 5.1. The vessel has a radius of 1 cm and is 20 cm long.

5.1.1.1 Stationary Flow

In this case a stationary flow in a straight cylindrical vessel is considered. The symmetry of the geometry and therefore the flow profile allow easy measurement of the computational savings while comparing the numerical solution obtained on different meshes to an analytical value. This example provides an opportunity to

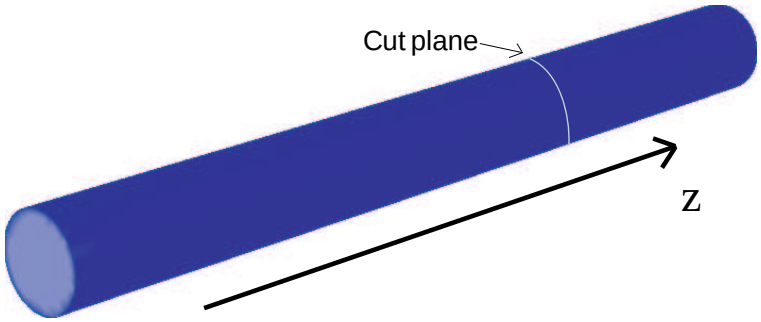

Figure 5.1: Model of a straight cylindrical blood vessel. The axis is aligned with the z direction.

explicitly quantify the major improvements achievable with our method.

The inlet flow profile is parabolic while the outflow has a zero natural pressure. The rigid vessel wall is assumed to have no-slip (zero velocity) boundary condition. The flow field is fully developed in the direction of the axis of vessel, varying only radially with a unit maximum. Therefore, the exact wall shear stress attains a constant value of $t_w = 2\mu$ over the entire vessel wall. In our example, the viscosity is set to $\mu = 0.01 dyn\ s/cm^2$ and the density is assumed to be $\rho = 1 g/cm^3$.

The comparison is based on results obtained on two kinds of meshes. First we obtain results on a series of successively refined uniform meshes, hereby reflecting the fact that the value should become more accurate the finer the mesh is. Second, we try to calculate the WSS more efficiently by applying anisotropic mesh adaptation based on the Hessian strategy. To perform anisotropic adaptation we compute the flow on the coarsest mesh and construct a mesh metric field based on the reconstructed second derivatives of the flow speed. The mesh metric obtained is input into the mesh adaptation module which, after a number of iteration cycles produces a highly anisotropic mesh. Fig. 5.2 shows the surface of three uniform meshes and an anisotropically adapted mesh.

Table 5.1 shows the mean values and standard deviations of WSS values that are interpolated on the surface mesh along a cut plane perpendicular to the axis of vessel, as indicated in Fig. 5.1, for different meshes. The mean values together with the standard deviations σ cover the analytic value in all the cases. Fluctuations of the WSS obtained on the uniform meshes are smaller the finer the mesh is. We

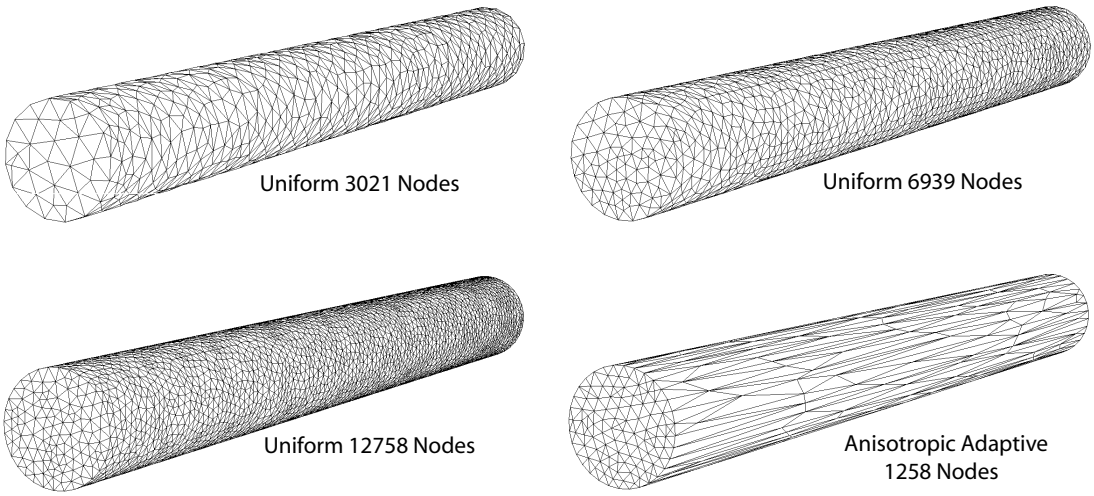

Figure 5.2: Surface mesh of three successively refined uniform meshes and one anisotropically adapted mesh for cylindrical vessel (mesh with 18K nodes is not shown in this figure).

observe that we achieve higher accuracy in terms of both the mean and the standard deviation when using an anisotropically adapted mesh of 1258 nodes as compared to a uniform mesh of 18184 nodes. Fig. 5.3 shows the spatial distribution of the WSS along the circumference of vessel wall at a fixed z location (see the cut plane depicted in Fig. 5.1.).

Table 5.1: WSS mean values and standard deviations (σ) for stationary flow in cylindrical vessel.

Mesh type	No. of nodes	Mean WSS	σ
Uniform	3021	1.975e-2	0.928e-3
Uniform	6939	1.977e-2	0.531e-3
Uniform	12758	1.982e-2	0.436e-3
Uniform	18184	1.985e-2	0.388e-3
Anisotropic	1258	1.991e-2	0.316e-3
Analytic	-	2.000e-2	-

We try to quantify the amount of savings that we gain through the adaptive method. We can claim, by considering the mean value along with the standard deviation as a measure, a gain factor of an order of magnitude when measuring computational expenses in terms of degrees of freedom. We should note that this

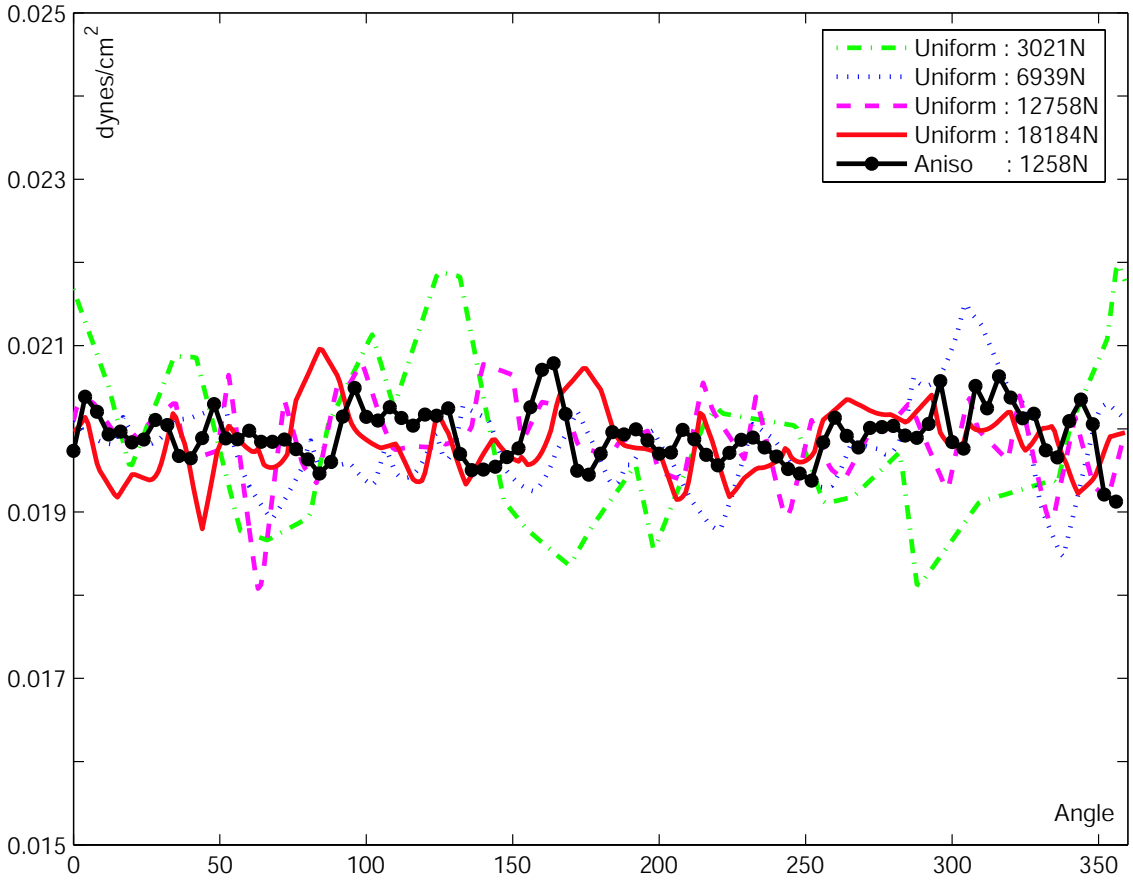

Figure 5.3: WSS values along the circumference of a cylindrical blood vessel for stationary flow.

gain factor has to be reduced when taking into account that first an initial solution has to be computed on the coarsest uniform mesh. However, the gain factors given above hold for the best case scenario where the flow solver scales linearly with the number of degrees of freedom. In practice, the computer time versus the number of unknowns varies by a higher order than linear which will enhance the gain factor. One can argue that in real cases it is likely that the flow will be much more complex than the one considered in this example but we expect anisotropic adaptivity to play a more important role for flows with confined critical regions, like sharp boundary layers near the walls, for which uniformly refined meshes over the whole domain would result in huge computational costs.

5.1.1.2 Pulsatile Flow

As blood flow is unsteady it is fruitful to understand the effect of pulsatile flow in the straight cylindrical blood vessel considered in the previous example. The time varying inflow boundary condition is assumed to be a Womersley profile [46], with Womersley number $\alpha = 5.6$ and a time period of 5s, for which the flow rate is depicted in Fig. 5.4. As in the previous example, we apply zero velocity (no-slip) boundary conditions on the vessel wall and zero natural pressure at the outlet. In this case, the viscosity and the density are assumed to be $\mu = 0.04 dyn\ s/cm^2$ and $\rho = 1 g/cm^3$, respectively.

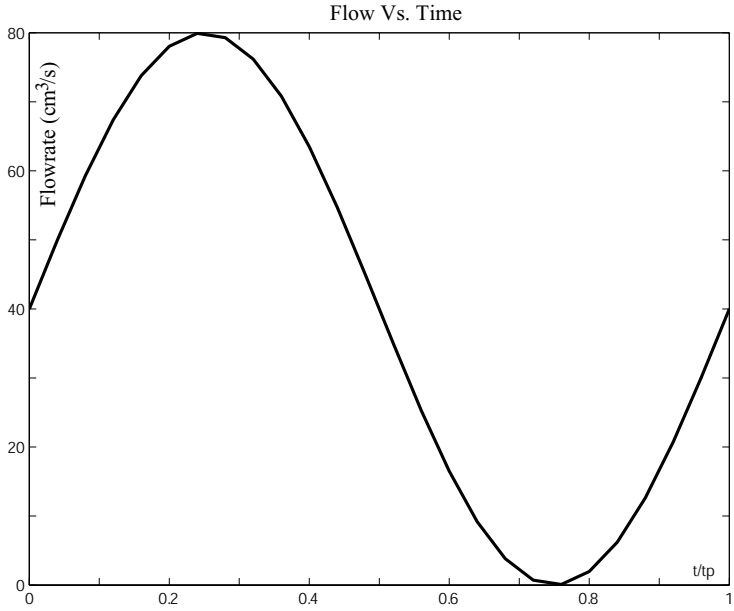

Figure 5.4: Flow rate profile at the inlet of a straight cylindrical vessel.

Similar to the stationary case, the only non-zero velocity component is along the axis of vessel. This component varies periodically in time at each location within the domain, reflecting the pulsatile nature of the flow. We analyze the WSS values both at a given point over a cycle and temporally averaged over the period. The latter is also known as the time average of the wall shear stress magnitude, defined as:

$$t_{mag} = \frac{1}{T} \int_0^T |\mathbf{t}_w| dt, \tag{5.1}$$

where, T is the time period of the cycle. t_{mag} is approximated in time by taking the discrete sum of the WSS values at each time step.

The comparison is again based on the results obtain on a series of uniformly refined meshes with those obtained on an anisotropically adapted mesh. As it does not seem to be advisable to adapt the mesh during the cycle for periodic flows we employ a single mesh adaptation for the whole cycle. To achieve this we use the time averaged flow speed over a cycle, i.e., we use the Hessians of the average flow field to construct the mesh metric field.

As can be expected, the adapted mesh looks similar to the ones depicted in Fig. 5.2. Table 5.2 lists the mean values of the time averaged t_{mag} along the wall circumference as depicted in Fig. 5.1 at a fixed z location. In this case we can use the analytical Womersley solution to compute the exact wall shear stress value and compare it with the numerical value.

Table 5.2: Time-averaged WSS magnitude (t_{mag}) mean values and standard deviations (σ) for pulsatile flow in cylindrical vessel.

Mesh type	No. of nodes	Mean t_{mag}	σ
Uniform	3021	2.8782	0.7638
Uniform	6939	2.8328	0.2630
Uniform	18184	2.6569	0.1612
Uniform	103409	2.5969	0.0451
Anisotropic	4238	2.6045	0.0504
Analytic	-	2.5900	-

Employing the anisotropic adaptive technique, again suggests a gain factor of an order of magnitude when considering the mean values along with the standard deviations of the time-averaged WSS magnitude. One can again argue that for real problems the flow will have more complexity but one would also expect the crucial flow features to be confined to a portion of the domain with different degrees of anisotropy. In other words, the flow considered in this and the previous example leads to mesh adaptation in the whole domain with essentially uniform refined of elements in the radial direction but real cases will most likely request a size field that will have significant variation of sizes in different directions and portions of the domain.

We further illustrate the benefit of anisotropic adaptation by presenting the time dependent behavior of the WSS magnitude at a specific point on the vessel wall in Fig. 5.5. While the shape of the curves follow the same pattern over a cycle, the magnitude is too high for the coarser meshes. When comparing to the analytical solution we can state that the anisotropic mesh is capable of adequately resolving the time dependent behavior. This shows that our adaptive strategy based on the average flow field for pulsatile flows is capable of producing a suitable mesh for the whole cycle to make accurate WSS predictions.

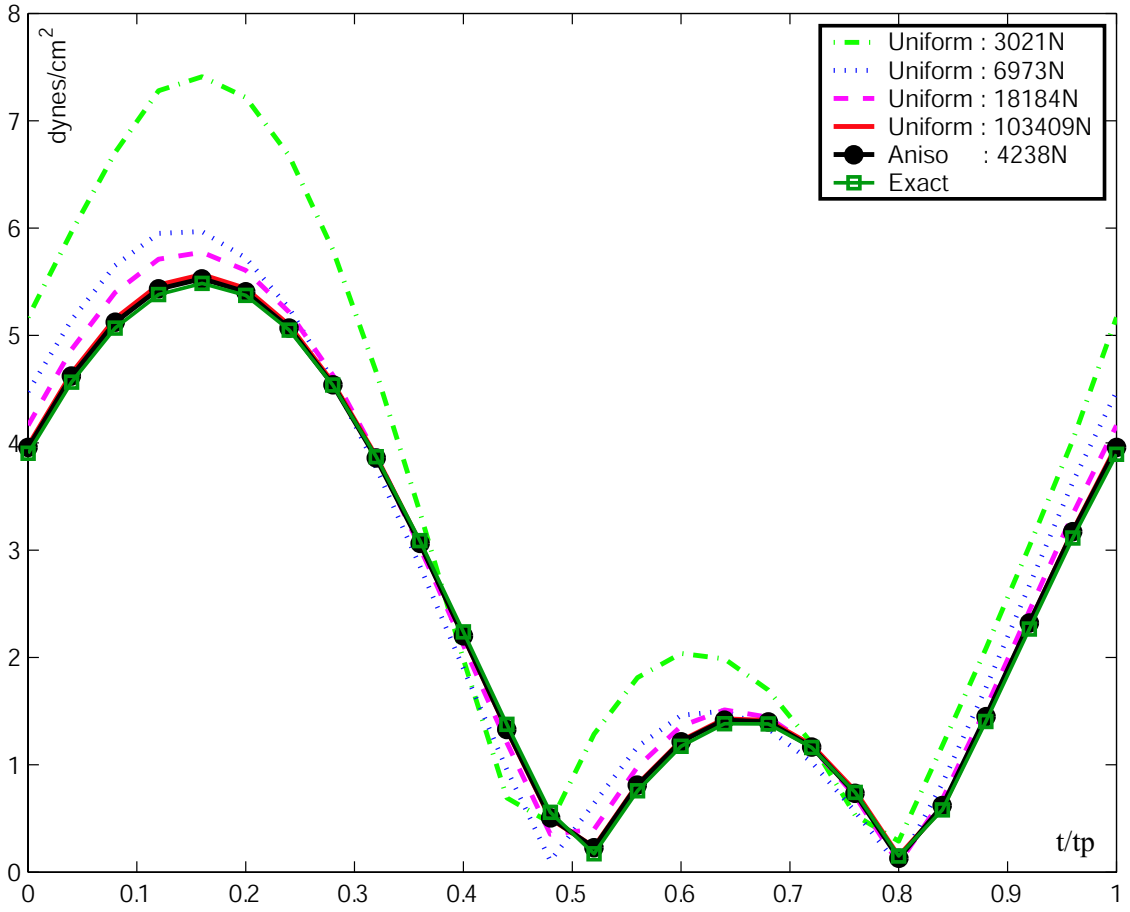

Figure 5.5: WSS values at a point on straight cylindrical vessel over a cycle for pulsatile flow.

5.1.2 Blood Vessel with Symmetric Bifurcation

In this example, the complexity in the blood vessel geometry is increased by introducing a symmetric bifurcation down the stream. The model for the blood vessel is depicted in Fig. 5.6.

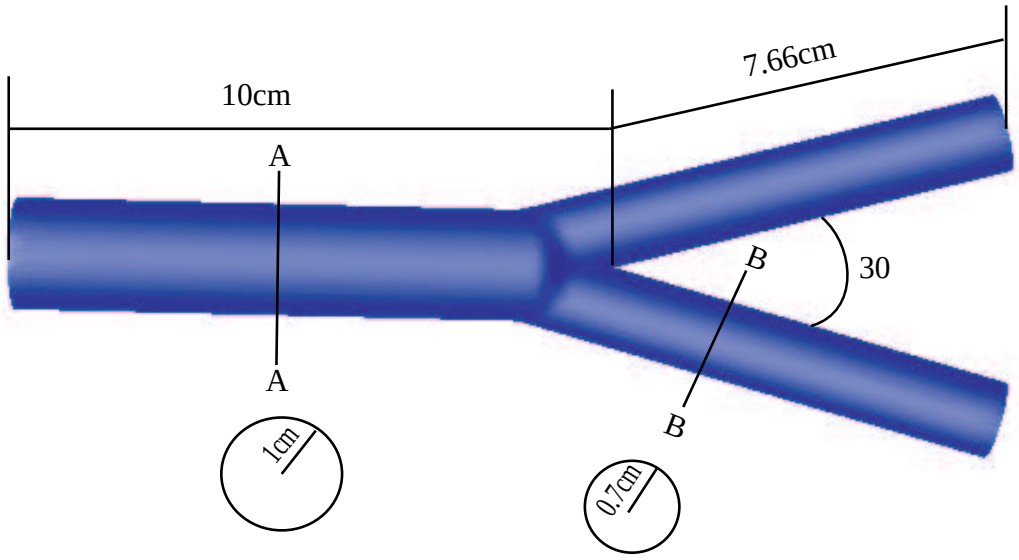

Figure 5.6: Model of a blood vessel with a symmetric bifurcation

In this case a stationary flow is considered. The inlet flow profile is taken to be an artificial turbulent flow profile based on Prandtl's one-seventh power law along the axis of vessel with high shear near the walls:

$$u = ((25(1-r))^{-2} + ((1-r)^{1/7})^{-2})^{-\frac{1}{2}}, \tag{5.2}$$

where, r (≤ 1) is the radial distance from the axis of vessel's main branch. In this example, the viscosity is set to a low value of $\mu = 10^{-5} dyn\ s/cm^2$ to avoid significant diffusion of the flow profile; and the density is assumed to be $\rho = 1 g/cm^3$

As before, we carry out simulations on different meshes to compare the results. Fig 5.7 shows four of the meshes used in this example together with their total number of nodes. A clip plane of the mesh illustrates the effect of mesh modification procedures, see Fig. 5.8. We observe that well aligned elements are created close to the vessel walls where the velocity gradient is steep. The flow field, as depicted in

Fig. 5.9, makes this observation more obvious. We also observe significant changes in the mesh close to the bifurcation. The element sizes in this region are small but isotropic (see the center zoom window in Fig. 5.8), reflecting the fact that the solution behavior is singular around bifurcation. This example shows the capability of our strategy to handle situations with arterial branching, i.e., it can automatically deal with cases requiring both isotropic and anisotropic adaptivity.

We show the computed WSS values along the circumference of the vessel wall in Fig. 5.10 at cross-section $A - A$, as depicted in Fig. 5.6. Similar to the case of straight cylindrical vessel we calculate the mean values along with the standard deviations σ of WSS (see, Table 5.3). The fluctuations in WSS values on uniform meshes are smaller the finer the mesh is. We observe that we achieve less fluctuation in WSS values on the adapted mesh. For this example we can claim, using mean value and standard deviation as a measure, a high gain factor of more than an order of magnitude.

Table 5.3: WSS mean values and standard deviations (σ) for stationary flow in blood vessel with symmetric bifurcation.

Mesh type	No. of nodes	Mean WSS	σ
Uniform	6767	1.0830e-3	9.1526e-4
Uniform	19055	0.6065e-3	5.1718e-4
Uniform	96818	0.4093e-3	4.1865e-4
Uniform	172232	0.3779e-3	3.2646e-4
Anisotropic	13811	0.2350e-3	0.8566e-4

5.1.3 Porcine Aorta

As the last but practically most relevant application we study the performance of our method by applying it to the simulation of pulsatile flow in a porcine aorta with a stenosis and a bypass graft. The dimensions of the model are approximately $10cm$ in length while the vessels diameter at the inlet is around $1.6cm$. Blood was modeled as an incompressible Newtonian fluid with a constant viscosity of $0.04dyn\ s/cm^2$ and a constant density of $1.06g/cm^3$. The geometric model is shown in Fig. 5.11.

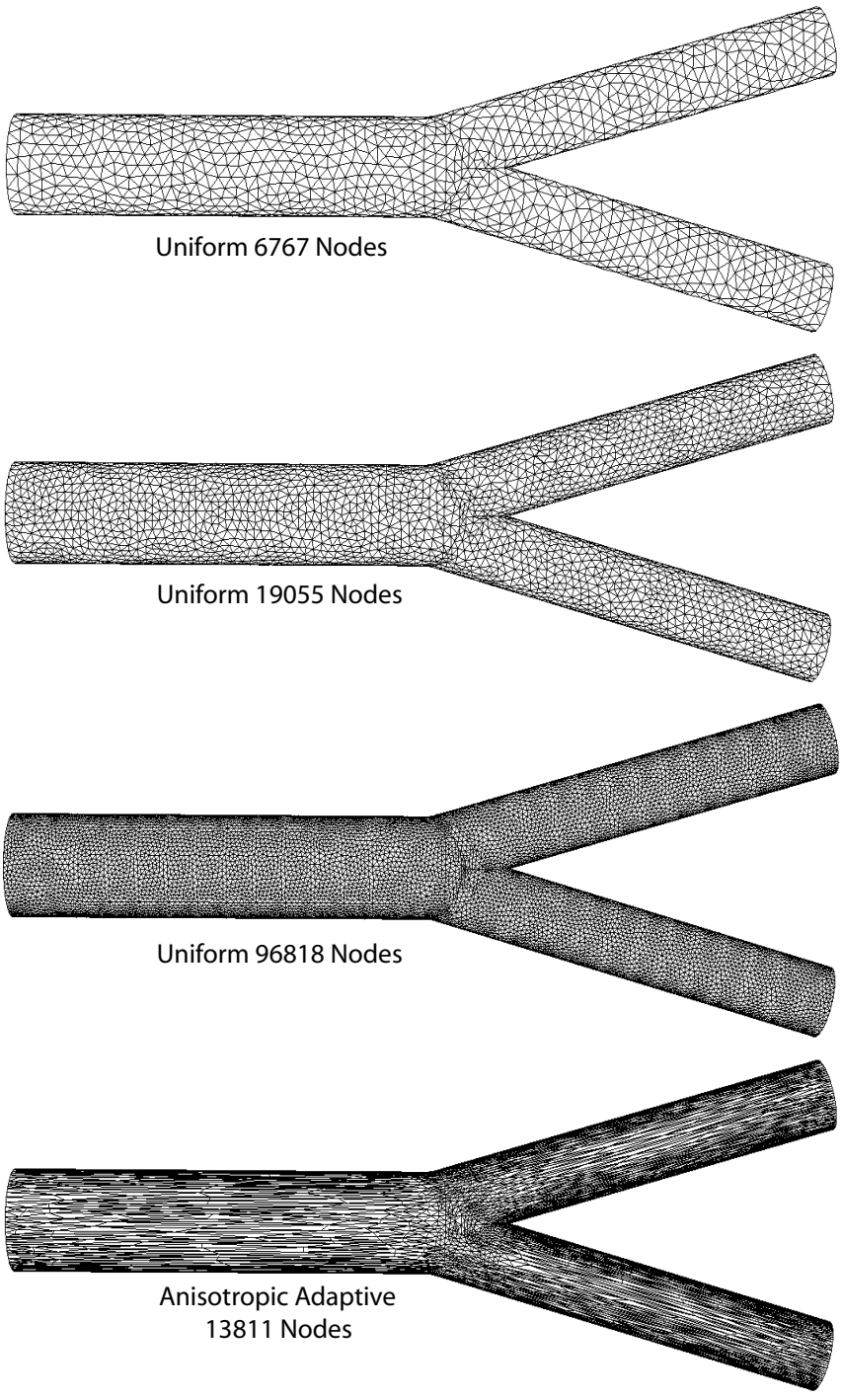

Figure 5.7: Surface mesh of three successively refined uniform meshes and one anisotropically adapted mesh for blood vessel with a symmetric bifurcation (mesh with 172K nodes is not shown in this figure).

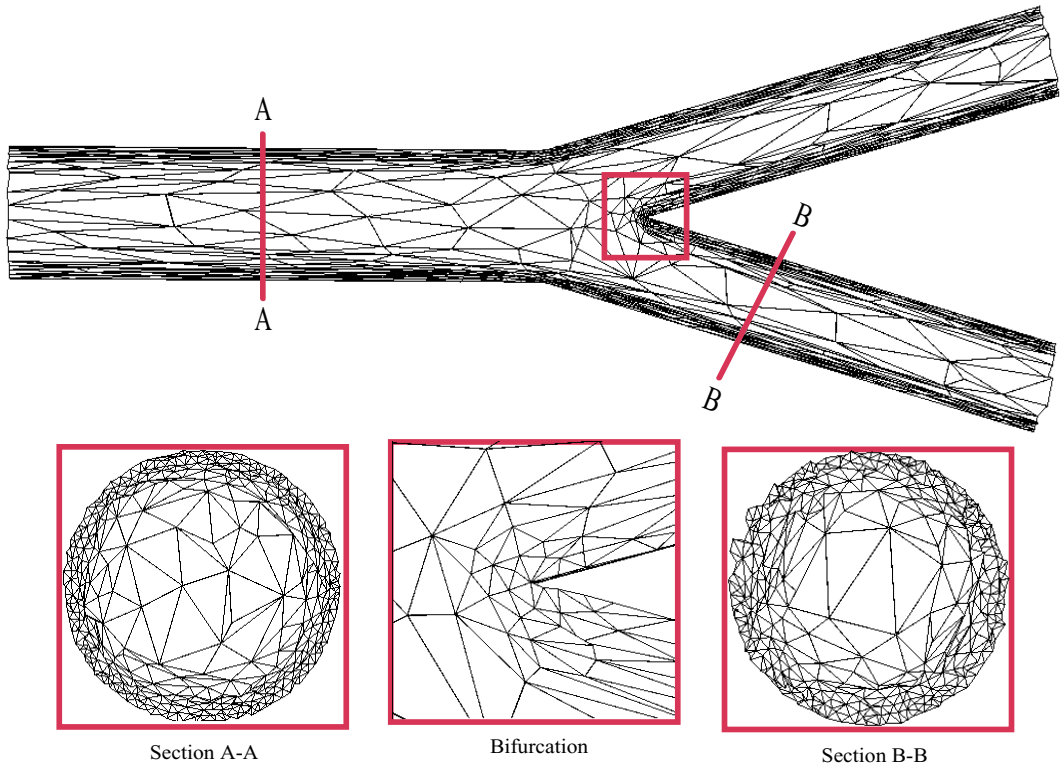

Figure 5.8: Clip plane through anisotropically adapted mesh of a blood vessel with a symmetric bifurcation (the windows correspond to zooms).

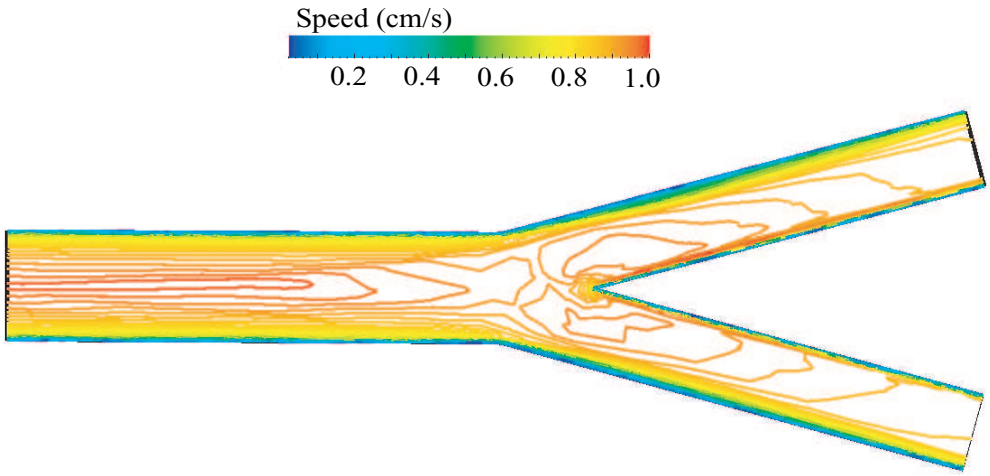

Figure 5.9: Isolines of flow speed on a clip plane in blood vessel with a symmetric bifurcation. Bright shades indicate high speed.

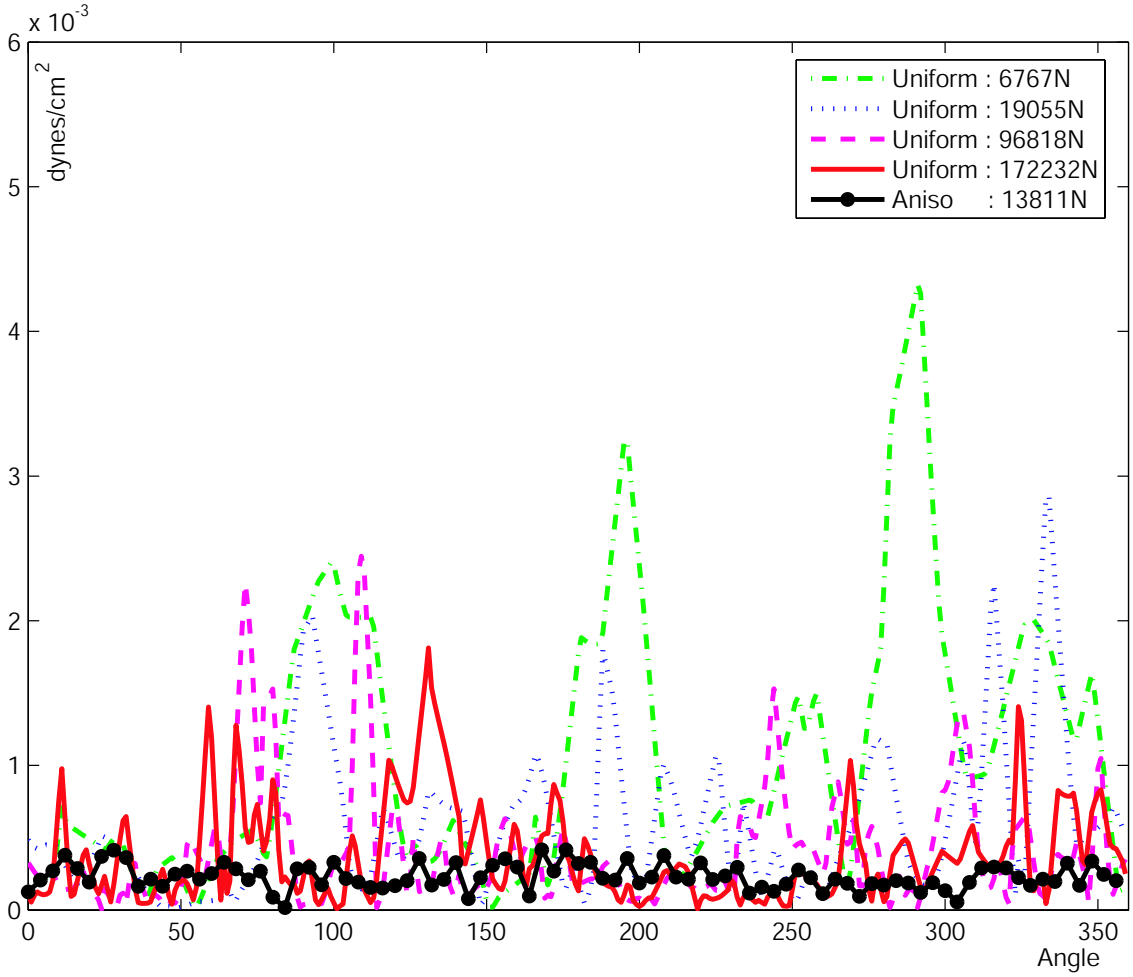

Figure 5.10: WSS values at section A-A in a blood vessel with a symmetric bifurcation.

The inlet is prescribed with a pulsatile flow profile that is based upon PC-MRI through-plane flow rate data, see [28]. Fig. 5.12 shows the velocity at an instant during the cardiac cycle and the inset depicts the velocity profile at a point near the center of the inlet for one cardiac cycle (together with the instant of the snapshot).

Similar to the other cases we obtain simulation results on different meshes, four of them being uniform and one being an anisotropically adapted mesh. Again, the latter was obtained by first computing the solution on the coarsest uniform mesh, then constructing the mesh metric field based on the Hessians of the averaged flow speed. Fig. 5.13 shows four of the meshes used in this simulation together with their total number of nodes.

Figure 5.11: Model of a porcine aorta with a stenosis bypassed by a graft.

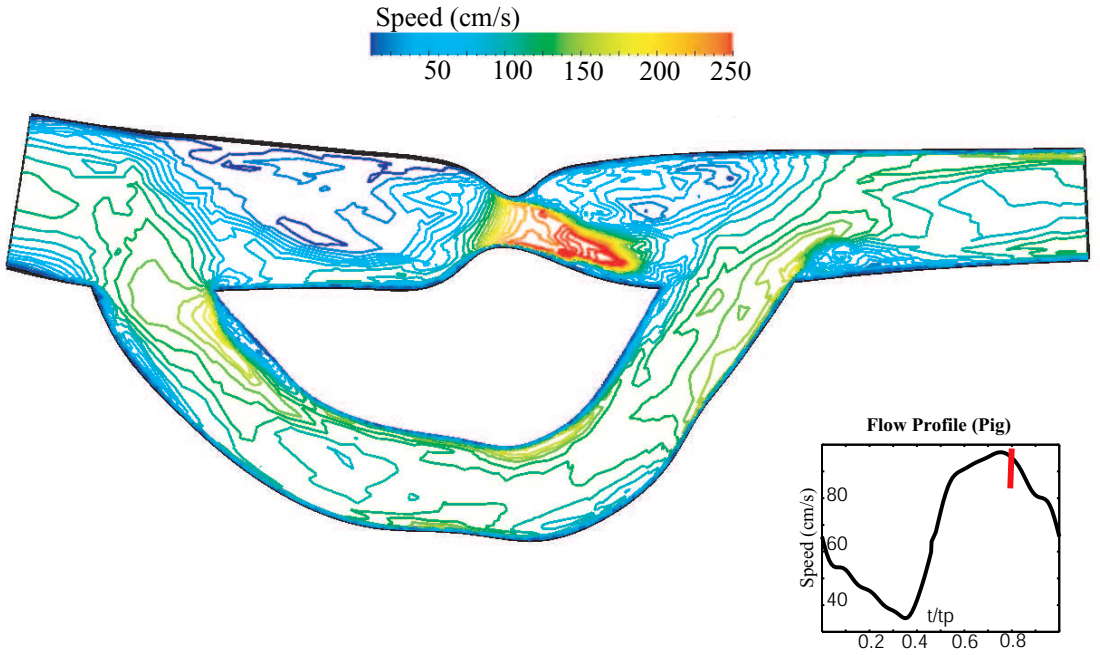

Figure 5.12: Flow profile during a cycle (inset) and isolines of flow speed on a clip plane in porcine aorta at an instant. Bright shades indicate high speed.

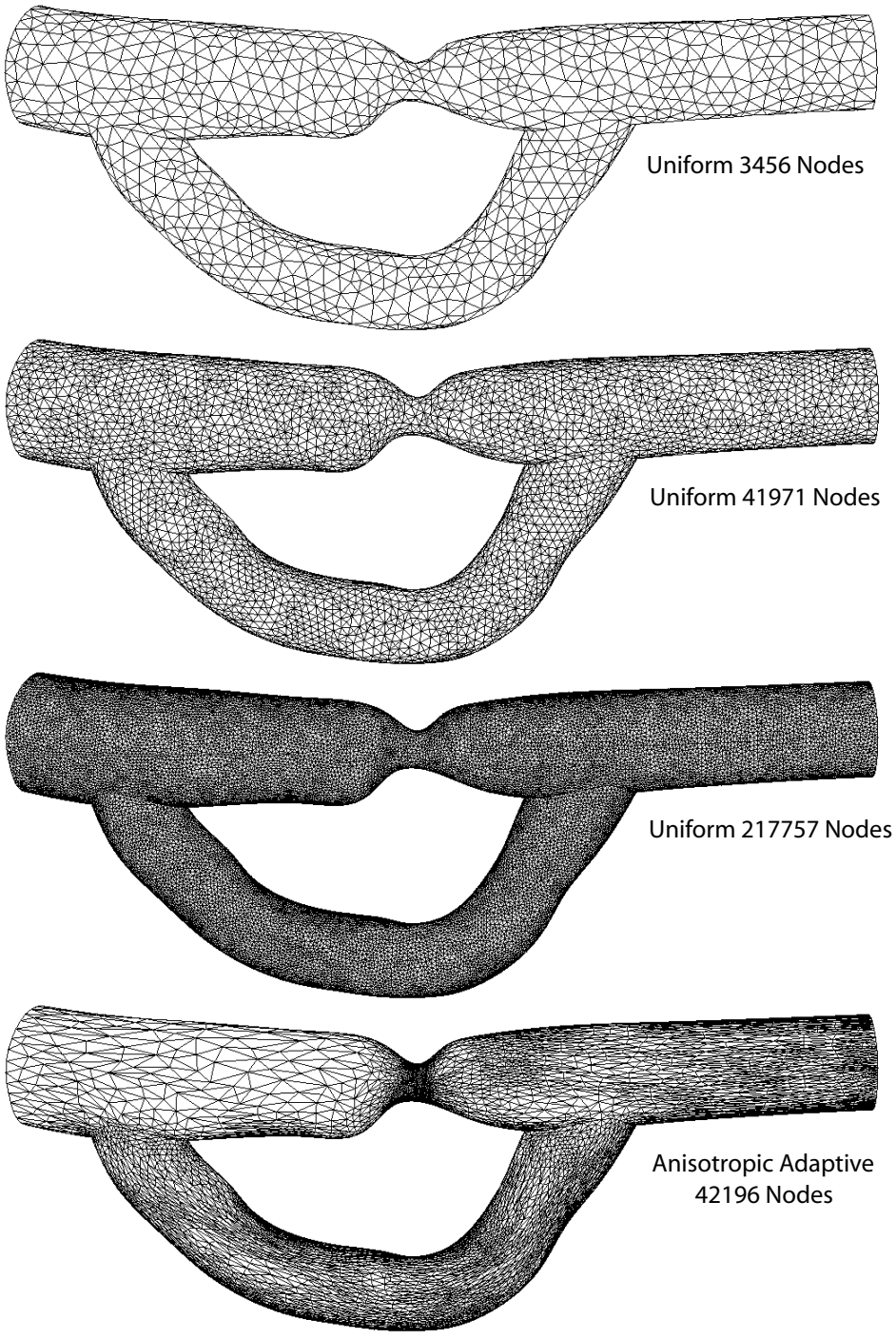

Figure 5.13: Surface mesh of three successively refined uniform meshes and one anisotropically adapted mesh for porcine aorta (mesh with 857K nodes is not shown in this figure).

A clip plane parallel to the flow direction of the main vessel further illustrates the effect of the mesh modification procedure, see Fig. 5.14. We observe that slender and elongated elements, well aligned with the flow features, are created such as the ones near the vessel walls due to the presence of boundary layer. This becomes more obvious when comparing Fig. 5.14 and the flow field at an instant as depicted in Fig. 5.12. Other regions where major mesh adaptation takes place (see the zoom windows in Fig. 5.14) are the stenosis area, re-entrant corners of the model and locations in the main artery where the re-directed flow impacts on the vessel wall. Typically, element sizes are predominately small but isotropic near the re-entrant corner, reflecting the fact that solution behavior around that portion is nearly singular.

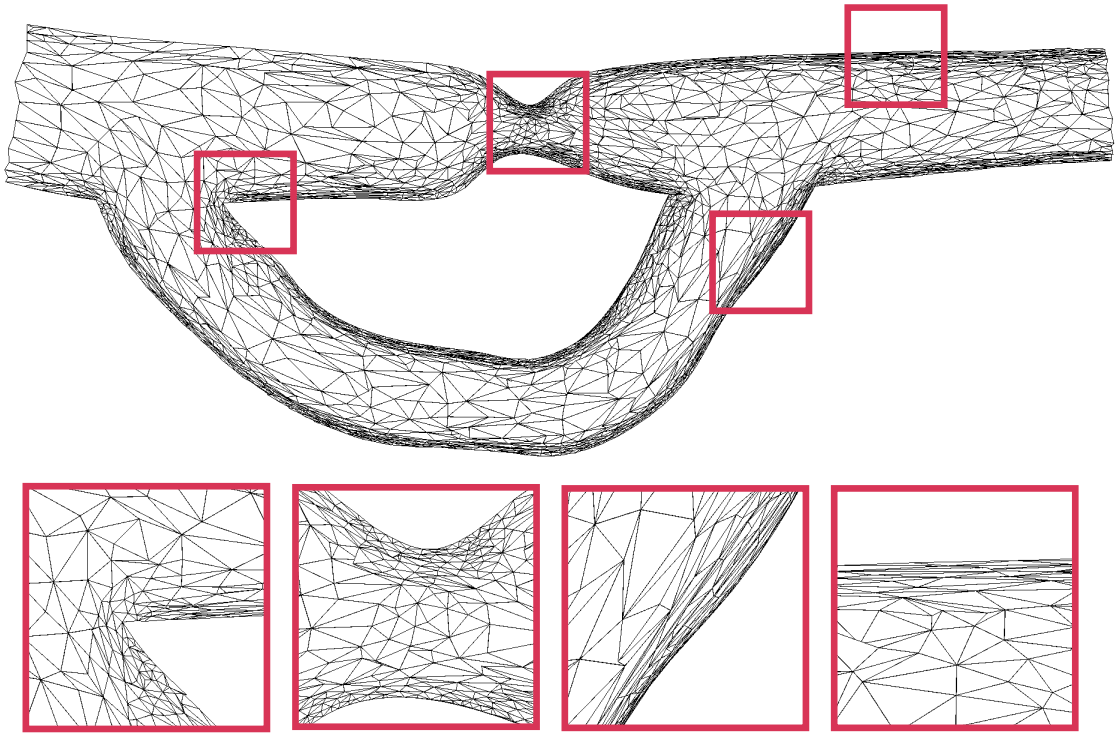

Figure 5.14: Clip plane through anisotropically adapted mesh of a porcine aorta (the windows correspond to zooms).

We analyze the transient behavior of the WSS in two different ways. First, we compare the WSS distribution for different meshes at the same instant during the cardiac cycle. Figs. 5.15 and 5.16 show the WSS at $t/tp = 0.2$ and $t/tp = 0.8$,

respectively. Secondly, in Fig. 5.17 we compare the time dependent behavior of the WSS for different meshes at one particular point on the vessel wall, located near the downstream vessel branching and labeled as P in Fig. 5.11. The WSS are computed on a series of uniform meshes ranging from 3456 nodes to over 857164 nodes and on an adapted mesh consisting of 42196 nodes.

The calculated WSS generally is too high on the coarser meshes, whereas the values show significant sign of convergence for the finer meshes. Even though the convergence is not uniform during the cardiac cycle we do observe convergence patterns that are similar to that of the pulsatile flow in the straight vessel case. For location P, see Fig. 5.17, considering that the finest uniform mesh of over 857K nodes (corresponding to over 4.7 million tetrahedra) sufficiently resolves all the flow features including the derivative quantities, we observe that the anisotropically adapted mesh follows the pattern of the finest uniform mesh very well in most parts of the cycle and differs only slightly in the rest of the cycle.

The convergence behavior for WSS seems sufficient for uniform meshes, i.e., the difference in WSS values between the meshes consisting of 857K and 217K nodes is extremely small as compared to the difference in WSS between meshes with 217K and 42K nodes for the whole cardiac cycle. The WSS values obtained on the anisotropically adapted mesh with 42K nodes follow those of the finest uniform mesh for most part of the cycle. The anisotropic mesh even seems to capture the WSS pattern better than the 217K mesh for a substantial part of the cycle. Considering the complex flow pattern resulting in a convergence behavior that cannot be fully classified as spatially and temporally uniform, which is further exacerbated by our attempt to reduce errors in WSS value at each point on the vessel walls, we still are able to claim considerable gains in computational time. In this example, it seems difficult to define a single gain factor for the whole spatial and temporal domain but we do observe that results are far better on anisotropically adapted meshes than those obtained on uniform meshes of twice or thrice the number of nodes and are similar to the finest uniform mesh with 857K nodes, i.e., 20 times the number of nodes, for a substantial part of both the spatial and temporal domain.

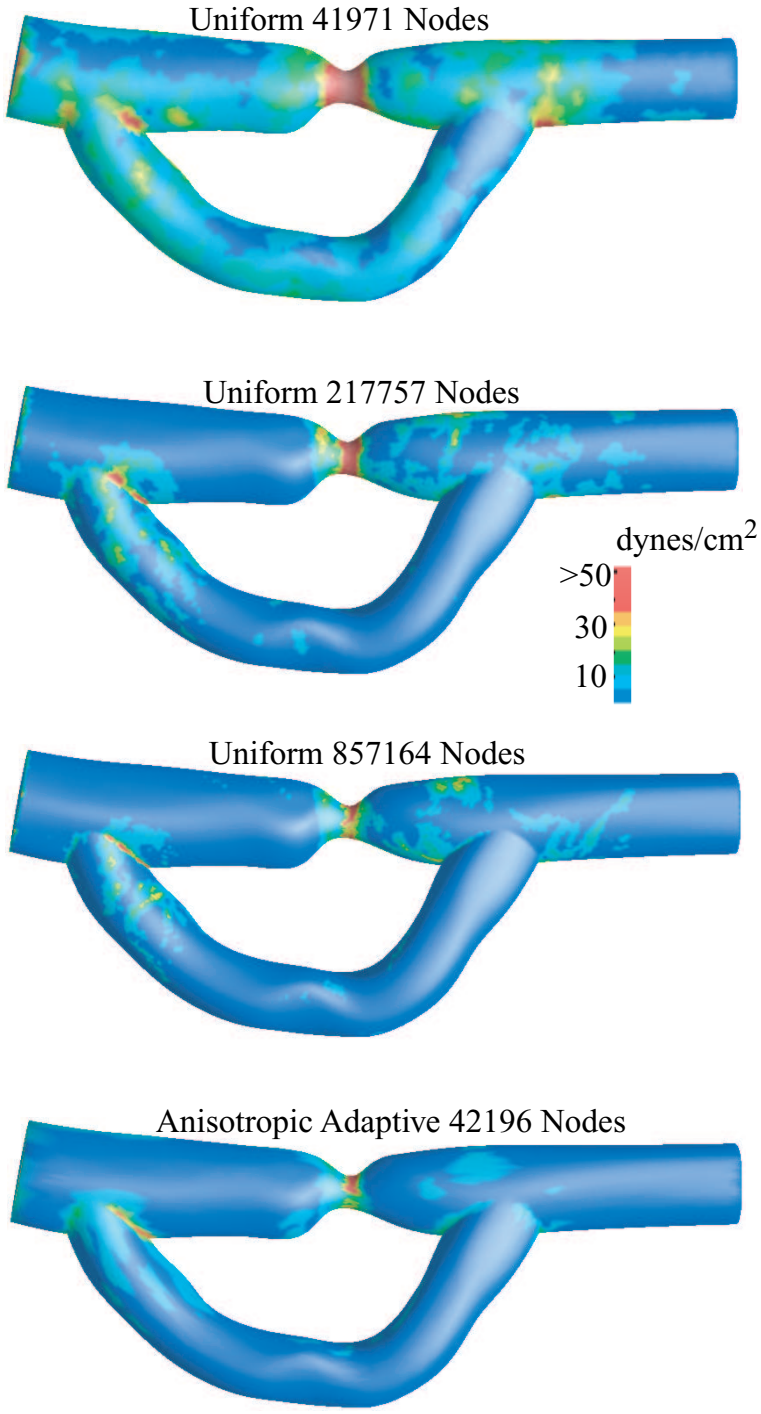

Figure 5.15: Wall shear stress at $t/tp = 0.2$ for porcine aorta.

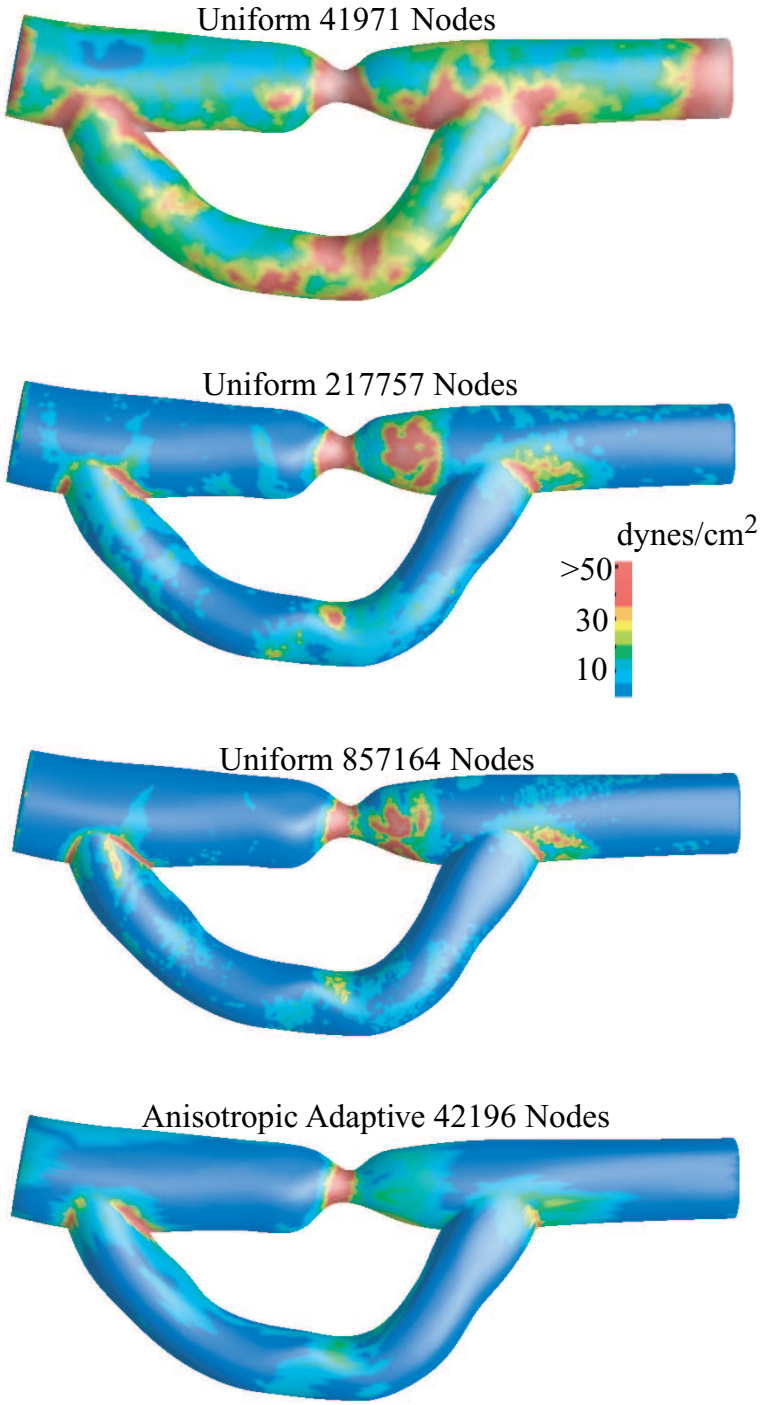

Figure 5.16: Wall shear stress at $t/tp = 0.8$ for porcine aorta.

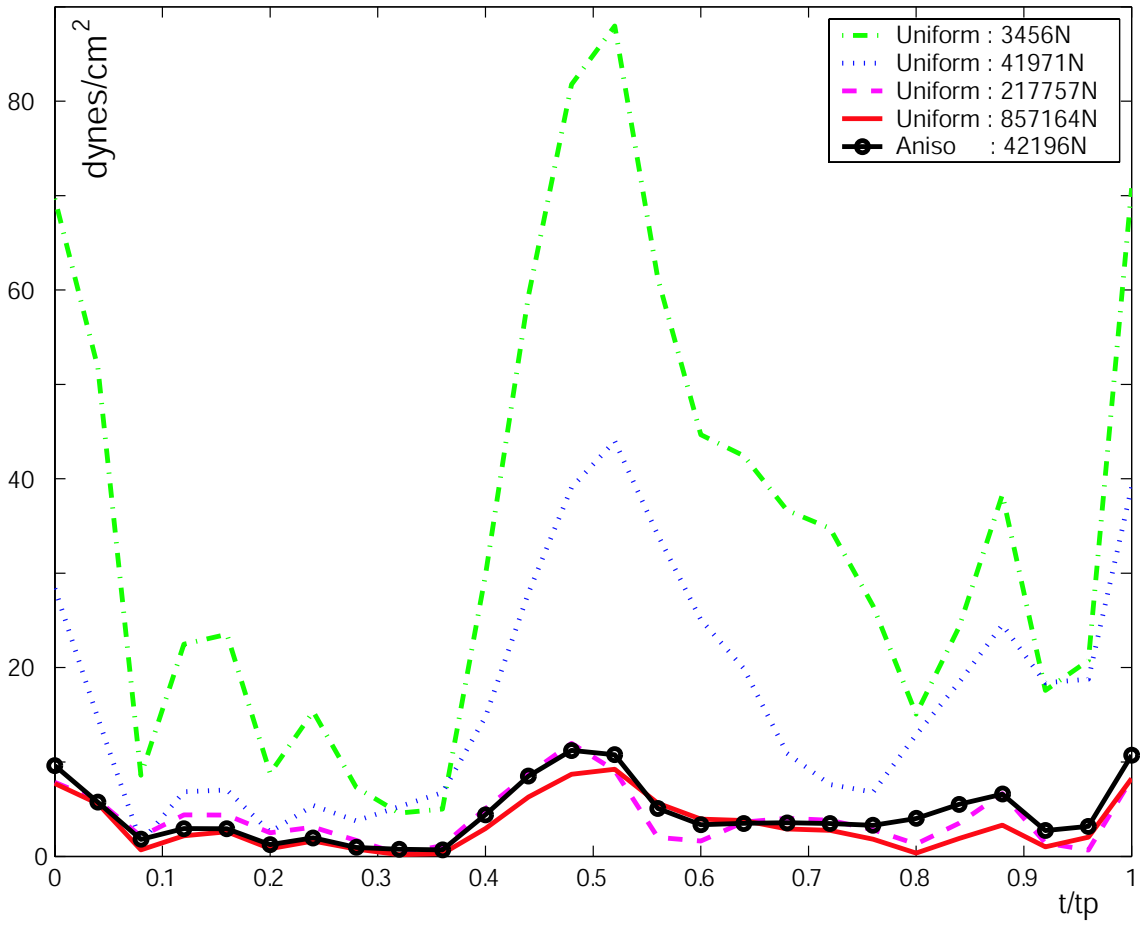

Figure 5.17: WSS during a cycle at a point P in porcine aorta.

5.2 Mesh Adaptation with Boundary Layer Mesh

In this section, we present results to show the impact of the mesh quality, close to the vessel walls, in WSS computation. To compare the results we apply two different meshing strategies. One in which meshes are obtained by performing complete anisotropic mesh adaptation process and other in which meshes are obtained by constraining the structured layer of elements for one (or two) layer(s) near the walls in the process of mesh adaptation.

We demonstrate this for two simple cases in which there is a steady flow with high shear near the walls. First we apply it to a simple case of a flow between parallel plates. In the second case, we consider a similar flow in a straight pipe. We use identical surface mesh for all the simulations in each example to see the effect of element size and shape in the direction normal to the walls.

5.2.1 Turbulent Channel

In this example, we consider a turbulent flow profile within a channel, i.e., a high shear flow between parallel plates. The viscosity is set to $\mu = 10^{-5} dyn\ s/cm^2$ and the density is assumed to be $\rho = 1 g/cm^3$. The model is depicted in Fig. 5.18 along with an inset that shows the inlet flow profile, as the one used in section 5.1.2.

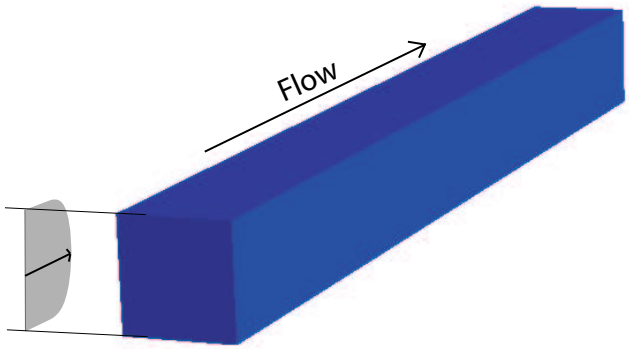

Figure 5.18: Model of a channel with inlet flow profile.

In this example, we obtain simulation results on three different meshes, one of them being a completely adapted mesh and others have structured elements frozen for one and two layer(s) near the walls. Fig. 5.19 shows the three meshes used in this simulation together with a zoom of meshes close to the wall. As before, the adaptation is based on the Hessian strategy.

As the domain is a polyhedron there is no geometric model approximation error. This case helps us to clearly isolate the mesh sensitivity in the post-processing step of WSS computation. We show WSS values on the upper surface of the channel at different locations along the length in Fig. 5.20. Table 5.4 provides the mean values along with the standard deviations of WSS for locations near the outflow, i.e., farther from the artificial inflow.

We can observe that oscillations in WSS prediction are reduced by an order of magnitude with the help of structured layer(s) of elements near the walls. Most of the fluctuations diminish even by one structured layer of elements. The differences in the prediction between the one and two structured layer(s) meshes vanish quickly with increase in downstream location. The results clearly demonstrate that the post-

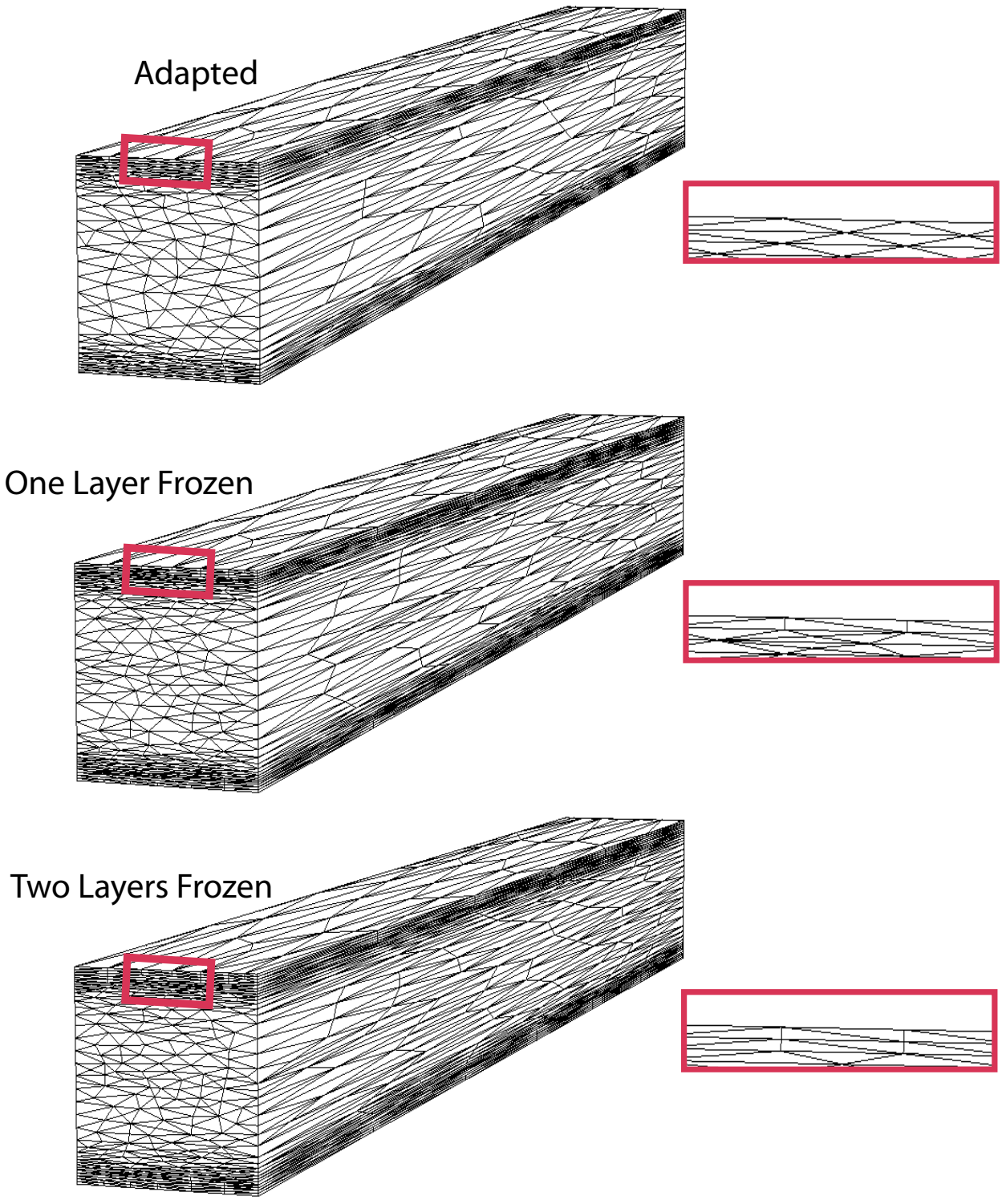

Figure 5.19: Three different meshes used for turbulent channel (the windows correspond to zooms).

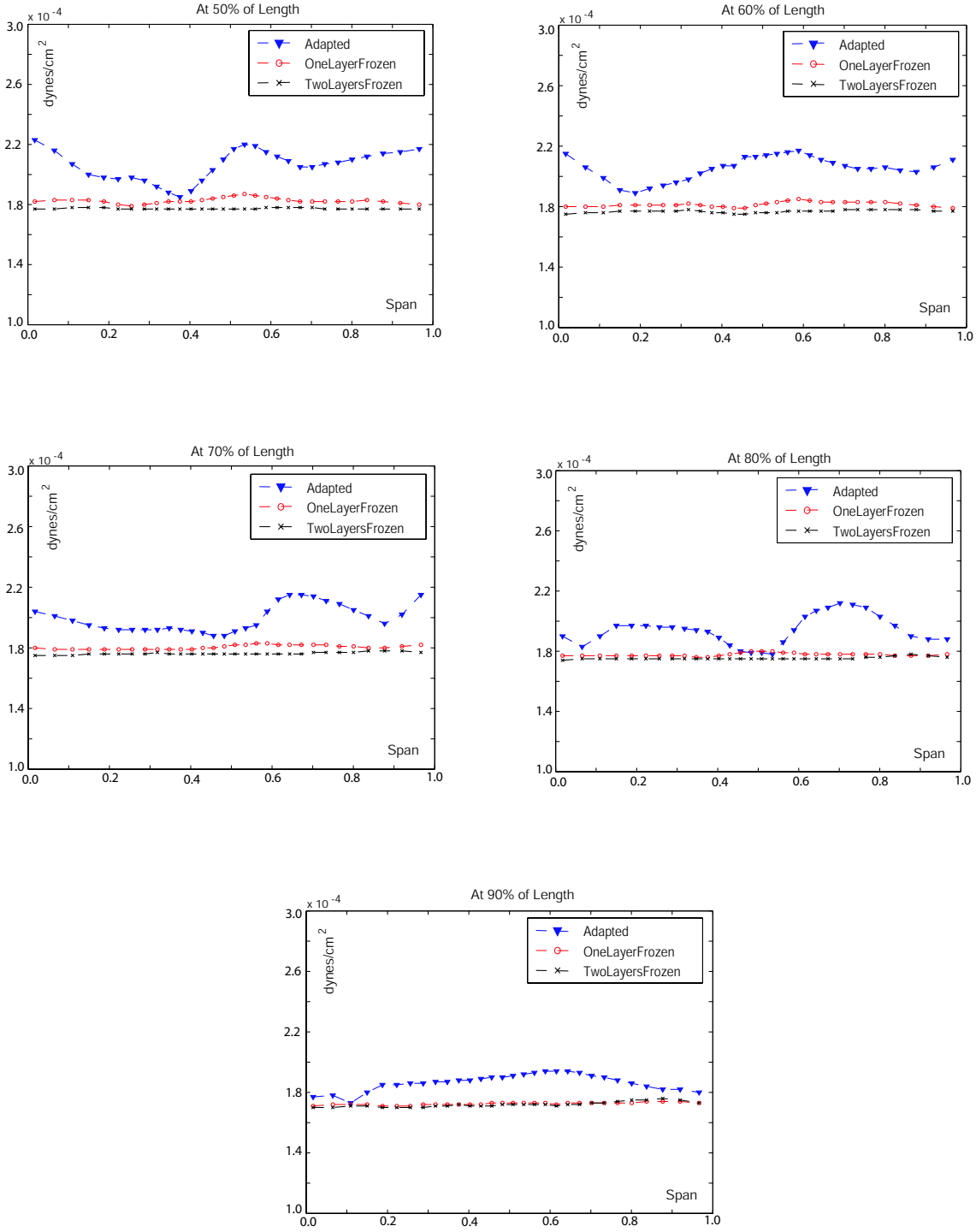

Figure 5.20: WSS values along the span on upper surface at different downstream locations for channel.

Table 5.4: WSS mean values and standard deviations (σ) for high shear flow in channel.

Mesh type	Mean WSS	σ
Adapted	1.9975e-4	1.9292e-5
One Layer Frozen	1.7931e-4	3.8245e-6
Two Layers Frozen	1.7559e-4	1.9011e-6

processing technique used for WSS computation is sensitive to the mesh quality close to the walls and shows that the WSS predictions can be significantly improved with the help of structured layer(s) of elements.

5.2.2 Turbulent Pipe

In this example, we consider a high shear flow in a straight cylindrical pipe. The value of the viscosity is set to $\mu = 10^{-5} dyn\ s/cm^2$ and the density is assumed to be $\rho = 1 g/cm^3$. The model is depicted in Fig. 5.21 along with an inset that depicts the inlet flow profile, which is an artificial turbulent flow profile based on Prandtl's one-seventh power law and is identical to the one used in section 5.1.2, see (5.2).

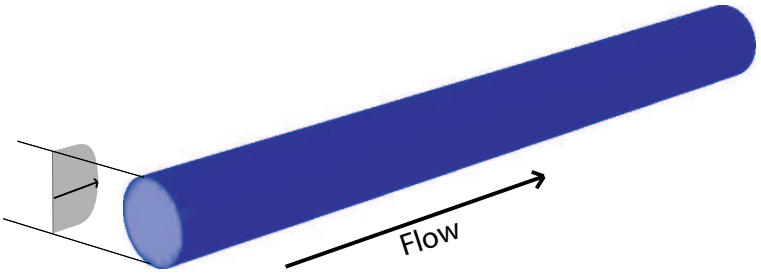

Figure 5.21: Model of a pipe with inlet flow profile.

As in the previous example we obtain simulation results on three different meshes (see, Fig. 5.22). We show the computed WSS values along the circumference of the pipe at different downstream locations in Fig. 5.23. Table 5.5 provides the mean values along with the standard deviations of WSS for locations near the outflow of the pipe, i.e., away from the artificial inflow.

Similar to the case of channel we observe that the oscillations in WSS prediction significantly reduces with the help of structured layer(s) of elements near the walls. Note that the fluctuations does not completely vanish with structured layers,

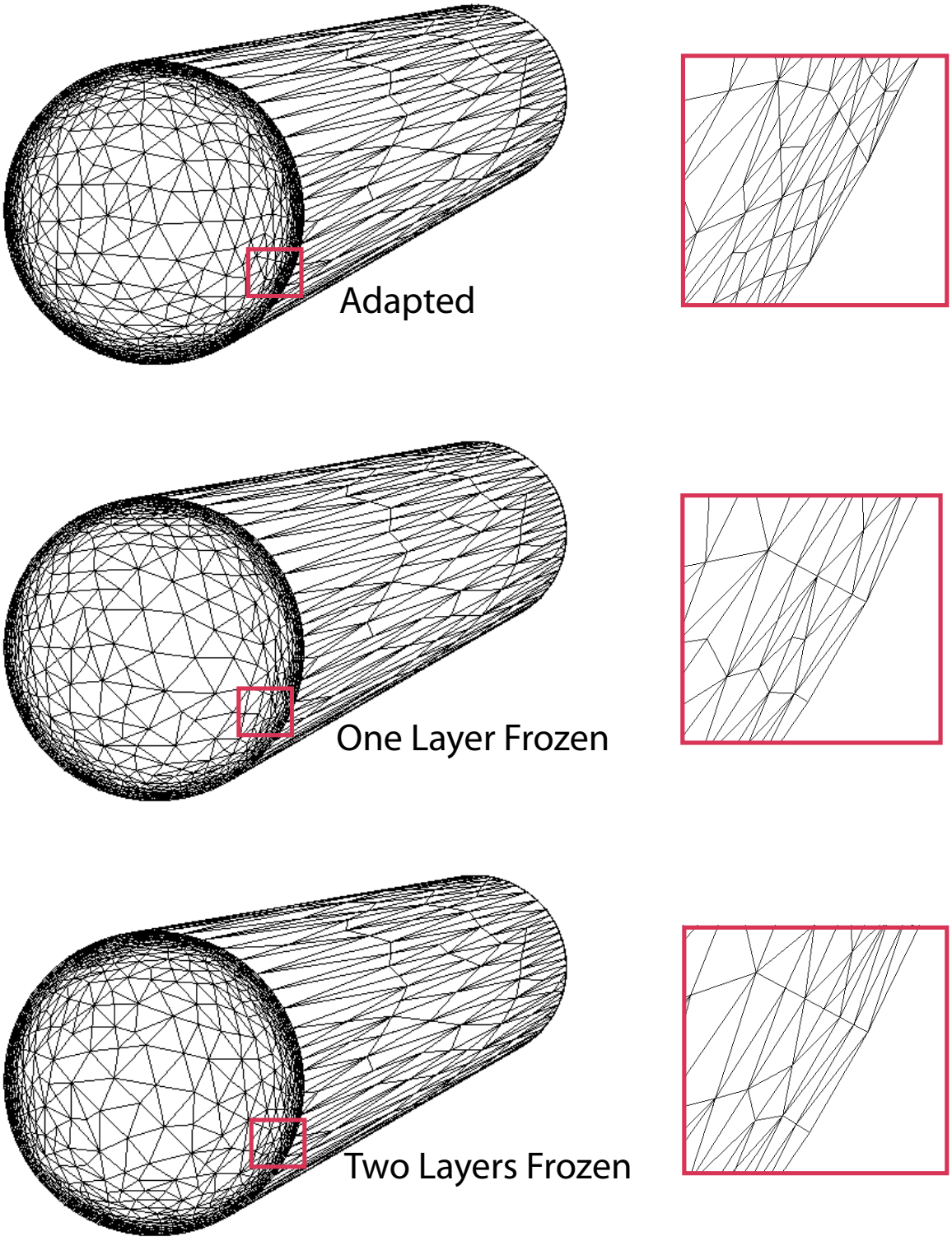

Figure 5.22: Three different meshes used for turbulent pipe (the windows correspond to zooms).

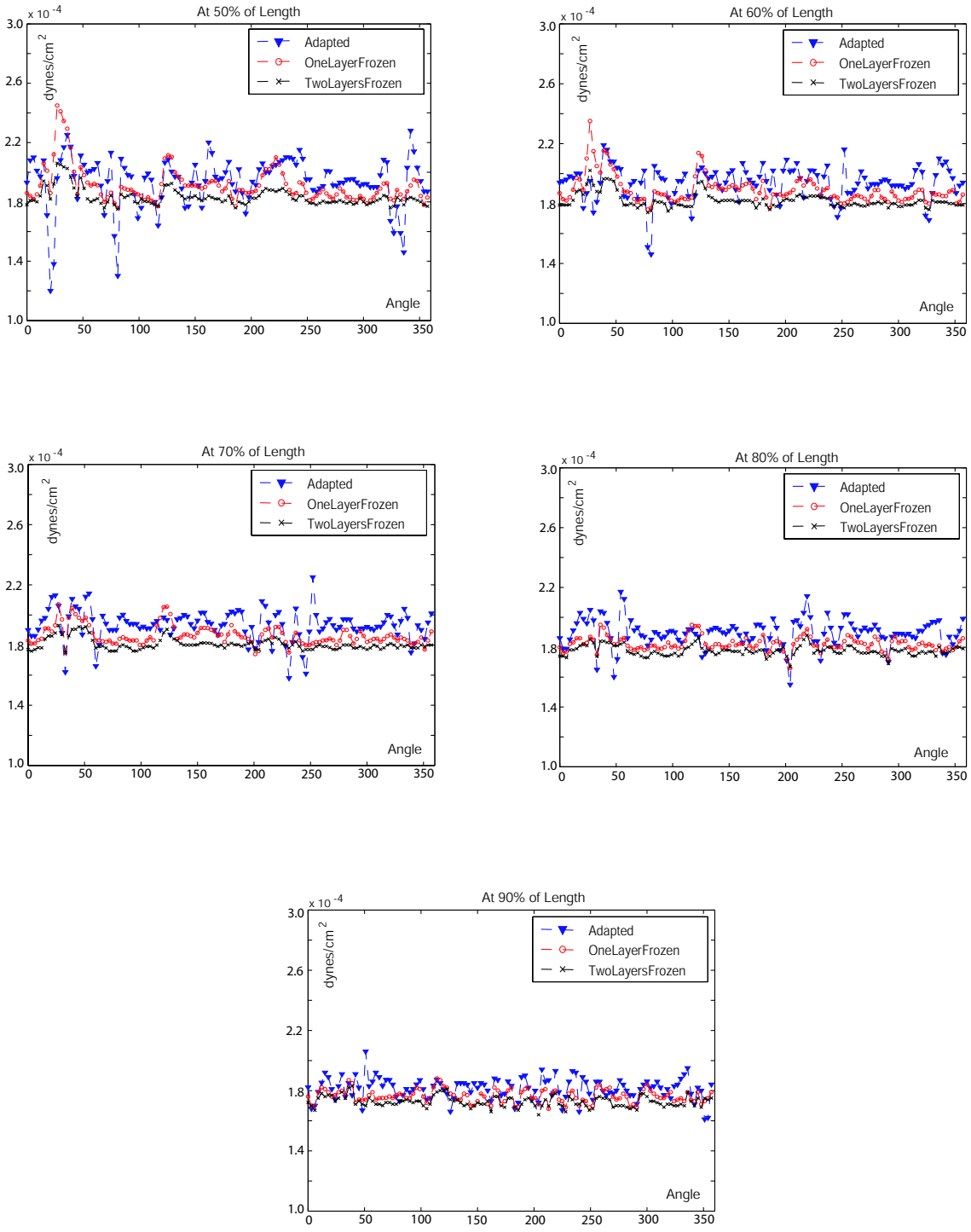

Figure 5.23: WSS values along the circumference at different downstream locations for pipe.

Table 5.5: WSS mean values and standard deviations (σ) for high shear flow in pipe.

Mesh type	Mean WSS	σ
Adapted	1.9139e-4	1.9857e-5
One Layer Frozen	1.8551e-4	1.1200e-5
Two Layers Frozen	1.7989e-4	6.1007e-6

owing to the fact that shear stress computation is also sensitive to the approximation of the geometric model (introduced due to linear straight sided elements). Again, the oscillations dampen out in the downstream direction. This example also shows that the structured layer(s) of elements near the walls helps to improve the WSS predictions substantially.

CHAPTER 6
SUMMARY AND FUTURE WORK

6.1 Conclusions

In this study, we have demonstrated a novel approach in the field of computational hemodynamics to perform efficient blood flow simulations. The method we presented is based on anisotropic mesh adaptivity dictated by directional error indicators defined from the interpolation part of the discretization error. The directional error indicators are used to construct a mesh metric field that yields information on the local mesh resolution desired in different directions. Mesh adaptation dictated by such a mesh metric field results in highly anisotropic meshes well aligned with the flow features leading to substantial computational savings. We applied our method to examples ranging from analytical cases to a real patient-specific one with different complexities in vessel geometries. With these examples we illustrated that our method can be applied to significantly accelerate hemodynamic finite element simulations.

In all the cases the quantity of physical interest studied was the wall shear stress. In these examples, we compared the wall shear stress predictions on the meshes produced through our anisotropic adaptive method to the ones computed on a series of uniformly refined meshes. We observed a gain factor of an order of magnitude for the two analytical examples. In the case of a blood vessel with a symmetric bifurcation a gain factor of more than an order of magnitude was noticed. Finally, we demonstrated our anisotropic adaptive procedure for numerical simulation of blood flow in a porcine aorta with a bypassed stenosis. In this example, it appeared rather difficult to define a single gain factor for the whole spatial and temporal domain but we do observe that results are far better on anisotropically adapted meshes than those obtained on uniform meshes of twice or thrice the number of nodes and are similar to the finest uniform mesh with 857K nodes, i.e., 20 times the number of nodes, for substantial part of both the spatial and temporal domain.

In this work, we also investigated the effect of mesh quality close to the walls

on the wall shear stress computation. We demonstrated that meshes with structured layers of elements at the walls lead to better wall shear stress predictions. We observed that the fluctuations in the predictions was higher by one order of magnitude on meshes without structured layers of elements in the case of channel flow; and was quadruple in the case of pipe flow for similar mesh resolution in the normal direction to the walls in each case.

6.2 Future Work

The current status of adaptive procedures clearly shows that although these procedures have been successfully applied for many interesting problems in varied areas of research, there are still open issues. These issues have to be resolved to design adaptive procedures applicable to more challenging problems, with complex geometries, possessing a large degree of anisotropy in solution characteristics. Automatically obtaining a suitable mesh for different quantities of physical interest not only requires focused effort to develop more sophisticated adaptive meshing techniques but also needs more stringent and dependable goal-oriented error estimators that can provide the necessary directional information.

Efficient and reliable large scale flow computations on geometries, like detailed human arterial system or complex aerospace geometries, deserve careful investigations to define the objectives of the adaptive procedures. Further, design and development of such indispensable tools would require necessary effort to achieve the goals, making such simulations practically plausible. Here, we try to present a few of the numerous research areas that need to addressed:

- To improve the computation of the boundary or wall quantities, like wall shear stress, pressure coefficients, eddy viscosity etc., requires structured and graded elements close to the walls. Development of adaptive meshing techniques that can create and/or maintain such elements for geometries with sharp corners or edges needs considerable efforts. Other possibility to improve the results in cases with curved geometries can be achieved by curving the structured and graded elements near the walls (see, for example [34]). One would expect better results on such meshes due to less geometric approximation errors that are

generally dominant near the boundaries; and also due to smooth surface normals that is possible by using C^1 elements. This process would not only require efforts to develop meshing techniques to create such elements but also need efforts to increase the capabilities of the flow solver and the post-processing step of boundary flux computation to handle such curved elements.

- To perform efficient simulations with high reliability demands more stringent error estimators. Real problems possessing large degrees of anisotropy, that are common in the field of fluid flows among many others, creates a desire for the estimation of the errors associated with different directions. Moreover, to improve the accuracy of a specific quantity of physical interest requires goal-oriented error estimators that will lead to further increase in the simulation efficiency (see, for example [37]). Design of such anisotropic goal-oriented error estimates require detailed error analysis based on the mathematical models of the problem at hand. Considerable efforts will be needed to investigate the effectiveness of such methods for real problems by carefully studying the convergence behavior of the errors.

- To practically achieve large scale computations, like high Reynolds number flow over complex aerospace geometries involving shocks and boundary layers, creates a critical need to properly link the two items mentioned above. The directional error estimates that have to be transformed into a size field information which can be fed to the mesh adaptation module must support strategies that can deal with the large variations of desired mesh sizes over the physical domain. In this regard, appropriate construction and usage of the size field information, over different portions of the domain, by the adaptive meshing techniques needs careful investigations.

- To extend the adaptive techniques mentioned above for problems involving several quantities of physical interest, for example, performing adaptation to obtain accurate predictions for both the wall shear stress and particle residence time, will require steps to construct a final size field based on the size fields associated with different quantities such that the errors are controlled within

the specified tolerance for each quantity. Such situations also oftenly arise in multi-physics problems.

- To better characterize hemodynamic flow simulations extension of the mathematical and constitutive models can be done to account for the many constituents of blood, like lipids, proteins. Application of improved boundary conditions accounting for vessel wall resistance will lead to more physical flow conditions. Other possibility to achieve better physiological conditions can be usage of models incorporating deformable blood vessels. Developments will be needed to be able to perform efficient simulations by using mesh adaptivity for deformable blood vessels that has temporal variability due to pulsatile nature of the blood flows.

REFERENCES

[1] M. Ainsworth and J. T. Oden. *A Posteriori Error Estimation in Finite Element Analysis*. John Wiley & Sons, New York, 2000.

[2] R. C. Almeida, R. A. Feijóo, A. C. Galeão, C. Padra, and R. S. Silva. Adaptive finite element computational fluid dynamics using an anisotropic error estimator. *Comp. Meth. Appl. Mech. Engng.*, 182:379–400, 2000.

[3] T. Apel and M. Dobrowolski. Anisotropic interpolation with applications to the finite element method. *Computing*, 47:277–293, 1992.

[4] E. Bänsch. Local refinements in 2 and 3 dimensions. *Impact of Comp. in Sci. and Engng.*, 3:181–191, 1991.

[5] H. Borouchaki, P.-L. George, and B. Mohammadi. Delaunay mesh generation governed by metric specifications. Part II. Applications. *Finite Elements in Analysis and Design*, 25:85–109, 1997.

[6] A. N. Brooks and T. J. R. Hughes. Streamline upwind / Petrov-Galerkin formulations for convection dominated flows with particular emphasis on the incompressible Navier-Stokes equations. *Comp. Meth. Appl. Mech. Engng.*, 32:199–259, 1982.

[7] G. C. Buscaglia and E. A. Dari. Anisotropic mesh optimization and its application in adaptivity. *Int. J. Numer. Meth. Engng.*, 40:4119–4136, 1997.

[8] M. J. Castro-Diáz, F. Hecht, B. Mohammadi, and O. Pironneau. Anisotropic unstructured mesh adaption for flow simulations. *International Journal of Numerical Methods in Fluids*, 25:475–491, 1997.

[9] P. G. Ciarlet. *The finite element method for elliptic problems*. North-Holland, Amsterdam, 1978.

[10] R. D. Cook, D. S. Malkus, and M. E. Plesha. *Concepts and Applications of Finite Element Analysis*. John Wiley & Sons, New York, 1999.

[11] H. L. de Cougny and M. S. Shephard. Parallel refinement and coarsening of tetrahedral meshes. *Int. J. Numer. Meth. Engng.*, 46:1101–1125, 1999.

[12] L. Formaggia and S. Perotto. New anisotropic a priori error estimates. *Numer. Math.*, 89:641–667, 2001.

[13] L. P. Franca and S. Frey. Stabilized finite element methods: II. The incompressible Navier-Stokes equations. *Comp. Meth. Appl. Mech. Engng.*, 99:209–233, 1992.

[14] P. J. Frey and F. Alauzet. Anisotropic mesh adaptation for transient flows simulations. In *Proc. 12th Internatinal Meshing Roundtable*, Santa Fe, NM, USA, 2003.

[15] P. J. Frey and F. Alauzet. Anisotropic mesh adaptation for CFD computations. *Comp. Meth. Appl. Mech. Engng.*, 2004. submitted.

[16] N. T. Frink. Assessment of an unstructured-grid method for predicting 3-D turbulent viscous flows. In *AIAA Paper 96-0292*, 1996.

[17] R. V. Garimella. *Anisotropic tetrahedral mesh generation.* PhD thesis, Rensselaer Polytechnic Institute, May 1999.

[18] R. V. Garimella and M. S. Shephard. Boundary layer mesh generation for viscous flow simulations. *Int. J. Numer. Meth. Engng.*, 49:193–218, 2000.

[19] P.-L. George. Tet meshing: construction, optimization and adaptation. In *Proc. 8th Internatinal Meshing Roundtable*, South Lake Tao, CA, USA, 1999.

[20] P. M. Gresho and R. L. Sani. *Incompressible Flow and the Finite Element Method.* Wiley, New York, NY, 1998.

[21] W. G. Habashi, J. Dompierre, Y. Bourgault, D. Ait-Ali-Yahia, M. Fortin, and M-G. Vallet. Anisotropic mesh adaptation: towards user-independent, mesh-independent and solver-independent CFD. Part I: general principles. *International Journal of Numerical Methods in Fluids*, 32:725–744, 2000.

[22] T. J. R. Hughes. *The finite element method: Linear static and dynamic finite element analysis*. Prentice Hall, Englewood Cliffs, NJ, 1987.

[23] T. J. R. Hughes, G. Engel, L. Mazzei, and M. G. Larson. The continuous Galerkin method is locally conservative. *Journal of Computational Physics*, 163:467–488, 2000.

[24] Y. Ito and K. Nakahashi. Unstructured mesh generation for viscous flow computations. In *Proc. 11th Internatinal Meshing Roundtable*, Ithaca, NY, USA, 2002.

[25] K. E. Jansen, M. S. Shephard, and M. W. Beall. On anisotropic mesh generation and quality control in complex flow problems. In *Proc. 10th Internatinal Meshing Roundtable*, Newport Beach, CA, USA, 2001.

[26] K. E. Jansen, C. H. Whiting, and G. M. Hulbert. A generalized-α method for integrating the filtered Navier-Stokes equations with a stabilized finite element method. *Comp. Meth. Appl. Mech. Engng.*, 190:305–319, 1999.

[27] A. Khawaja and Y. Kallinderis. Hybrid grid generation for turbomachinery and aerospace applications. *Int. J. Numer. Meth. Engng.*, 49:145–166, 2000.

[28] J. P. Ku, M. T. Draney, F. R. Arko, W. A. Lee, F. P. Chan, N. J. Pelc, C. K. Zarins, and C. A. Taylor. In vivo validation of numerical prediction of blood flow in arterial bypass grafts. *Ann. Biomed. Eng.*, 30:743–752, 2002.

[29] G. Kunert. Toward anisotropic mesh construction and error estimation in the finite element method. *Numer. Methods Partial Differential Equations*, 18:625–648, 2002.

[30] X. Li. *Mesh modification procedures for general 3-D non-manifold domains*. PhD thesis, Rensselaer Polytechnic Institute, Aug. 2003.

[31] X. Li, M. S. Shephard, and M. W. Beall. 3D anisotropic mesh adaptation by mesh modifications. *Comp. Meth. Appl. Mech. Engng.*, 2003. submitted.

[32] X. Li, M. S. Shephard, and M. W. Beall. Accounting for curved domains in mesh adaptation. *Int. J. Numer. Meth. Engng.*, 58:247–276, 2003.

[33] R. Löhner and J. Cebral. Generation of non-isotropic unstructured grids via directional enrichment. *Int. J. Numer. Meth. Engng.*, 49:219–232, 2000.

[34] X.-J. Luo, M. S. Shephard, R. M. O'Bara, R. Nastasia, and M. W. Beall. Automatic p-version mesh generation for curved domains. *Engineering with Computers*, 20:273–285, 2004.

[35] C. C. Pain, A. P. Umpleby, C. R. E. de Oliveira, and A. J. H. Goddard. Tetrahedral mesh optimisation and adaptivity for steady-state and transient finite element calculations. *Comp. Meth. Appl. Mech. Engng.*, 190:3771–3796, 2001.

[36] S. Prakash and C. R. Ethier. Requirements for mesh resolution in 3D computational hemodynamics. *J. Biomech. Eng.*, 123:132–144, 2001.

[37] S. Prudhomme and J. T. Oden. On goal-oriented error estimation for elliptic problems: application to the control of pointwise errors. *Comp. Meth. Appl. Mech. Engng.*, 176:313–331, 1999.

[38] J. F. Remacle, X. Li, N. Chevaugeon, and M. S. Shephard. Transient mesh adaptation using conforming and non conforming mesh modifications. In *Proc. 11th Internatinal Meshing Roundtable*, Ithaca, NY, USA, 2002.

[39] J. F. Remacle, X. Li, M. S. Shephard, and J. E. Flaherty. Anisotropic adaptive simulation of transient flows using Discontinuous Galerkin methods. *Int. J. Numer. Meth. Engng.*, 2003. submitted.

[40] Farzin Shakib. http://www.acusim.com.

[41] P. R. Spalart and S. R. Allmaras. A one-equation turbulence model for aerodynamic flows. In *AIAA Paper 92-439*, 1992.

[42] B. Szabo and I. Babuška. *Finite Element Analysis*. Wiley, New York, 1991.

[43] C. A. Taylor, T. J. R. Hughes, and C. K. Zarins. Finite element modeling of blood flow in arteries. *Comp. Meth. Appl. Mech. Engng.*, 158:155–196, 1998.

[44] R. Verfürth. *A Review of Posteriori Error Estimation and Adaptive Mesh-Refinement Techniques*. Teubner-Wiley, Stuttgart, 1996.

[45] C. H. Whiting and K. E. Jansen. A stabilized finite element method for the incompressible Navier-Stokes equations using a hierarchical basis. *International Journal of Numerical Methods in Fluids*, 35:93–116, 2001.

[46] J. Womersley. Method for the calculation of velocity, rate of flow and viscous drag in arteries when the pressure gradient is known. *J. Physiol. (London)*, 127:553–563, 1955.